22. Surface-Tension-Induced Convection

Experiment MA-041

R. E. Reed,[†] W. Uelhoff,[a] and H. L. Adair[b]

ABSTRACT

This experiment was designed to detect possible convection caused by a steplike compositional variation in a liquid metal in a microgravity environment. Wetting and nonwetting ampoules were used to determine the extent of the stirring effects if they were present. Because stirring effects can be caused by temperature gradients, the temperature gradients for this experiment were minimized.

Steplike compositional variation was created by pressure bonding a lead-gold alloy (0.05 atomic percent gold) to pure lead. Two diffusion temperatures (923 and 723 K) were used; if no stirring effects were present, it was hoped that the liquid diffusion parameters for gold in lead could be obtained. Convection effects were observed but were not sufficiently large to bring about total mixing in the space-flight specimens. However, they were large enough to prohibit analysis of the pure diffusion process. The most plausible explanation for the flow phenomena observed is convection induced by the Marangoni effect.

Two identical experimental arrangements were used to compare the transport mechanisms of gold in liquid lead in unit gravity and microgravity environments.

INTRODUCTION

In the absence of gravity, stirring in a liquid due to density differences caused by thermal or compositional gradients is suppressed. However, other mechanisms resulting in natural convection in a microgravity environment exist and have been described elsewhere (ref. 22-1). One of the most important mechanisms for liquid metals is surface-tension-driven convection (Marangoni effect), which may become predominant in a low-gravity environment. In this case, surface tension differences caused by compositional or temperature gradients have been demonstrated to cause stirring in liquids during experiments performed onboard the Skylab spacecraft. Compositional gradients were created by adding soap solution or grapejuice to a large water globule. The result was a vigorous fluid motion for some moments after the addition. Also, evidence of stirring was detected in the sphere-forming (ref. 22-2) and welding (ref. 22-3) experiments involving electron beam heating; this type of heating causes very steep temperature gradients.

Experiment MA-041 was designed to detect possible convection caused by steplike compositional variation in a liquid metal contained in both wetting and nonwetting ampoules. The general concept of the investigation was to set up a liquid diffusion couple of lead (Pb) and Pb-0.05 atomic percent (at.%) gold (Au) alloy in a microgravity environment. The couples were to be maintained in the molten state for approximately 2 hours, during which the Au would diffuse a distance of approximately 2.5 cm. If there were no convective

---

[†]Principal Investigator (deceased).

[a]Institut fur Festkörperforschung, Kernforschungsanlage Jülich, German Federal Republic.

[b]Oak Ridge National Laboratory.

stirring effects between the Pb and the Pb-0.05 at.% Au alloy, a normal concentration-distance profile for Au would be found in the diffusion couples. The use of two diffusion temperatures (923 and 723 K) should enable estimation of the liquid diffusion parameters for Au in Pb. The existence of convective stirring effects should be revealed by means of the autoradiographic technique used for the diffusion analysis. The extent of the convective stirring effects (if present) were to be determined by examination of the wetting and nonwetting containers.

Surface-tension-induced convection could be expected if the specimens were not in contact with the ampoule walls. However, if the specimens touch the walls, the interface tension between the alloy and pure Pb should not be able to create a convection effect according to the fluid dynamic theories by which zero flow is expected at the walls (ref. 22-4). On the other hand, a zinc (Zn) self-diffusion experiment (ref. 22-5) indicated that slight convection occurred in liquid Zn contained in a nonwetting capsule that was heated in a temperature gradient of approximately 45 K/cm. The change in surface tension (not interface tension) with temperature for Zn has been reported to be in the range of -0.009 to -0.025 $\mu J/cm^2$ K (-0.09 to -0.25 erg/cm^2 K) (ref. 22-6, pp. 403 and 404). Therefore, a surface tension change of approximately 0.5 to 1.5 percent/cm could have occurred in the Zn self-diffusion experiment.

THE LEAD-GOLD SYSTEM

A Pb/Pb-0.05 at.% Au diffusion couple was selected for this experiment for three major reasons.

1. The melting point of Pb (600 K) was sufficiently low to provide a convenient temperature range for liquid diffusion and to ensure that 0.05 at.% Au would be initially soluble in Pb upon solidification. Any subsequent precipitation of Pb_2Au would be *in situ* and thus would still provide a marker for the original position of the Au. If the precipitation reaction were sufficiently sluggish, the Au could be in solid solution at room temperature. Figure 22-1 is the portion of the Pb-Au phase diagram of interest in this experiment. The calculated solubility line (curve) shown in figure 22-1 is based on data from reference 22-7.

2. The nuclear properties of Pb and Au make the mixture an ideal diffusion couple to study by neutron activation techniques. The distribution of Au in the Pb matrix can be determined autoradiographically. In this case, samples were neutron irradiated in the center hole of the Bulk Shielding Reactor deuterium oxide tank at Oak Ridge National Laboratory (ORNL) in essentially a pure thermal flux of 1.2×10^{12} neutrons sec^{-1} cm^{-2}. The nuclear data of interest for Pb and Au are shown in table 22-I. After neutron activation, the Au distribution was determined by placing a polished section of the sample on a nuclear emulsion plate that is sensitive to 0.96-MeV electrons.

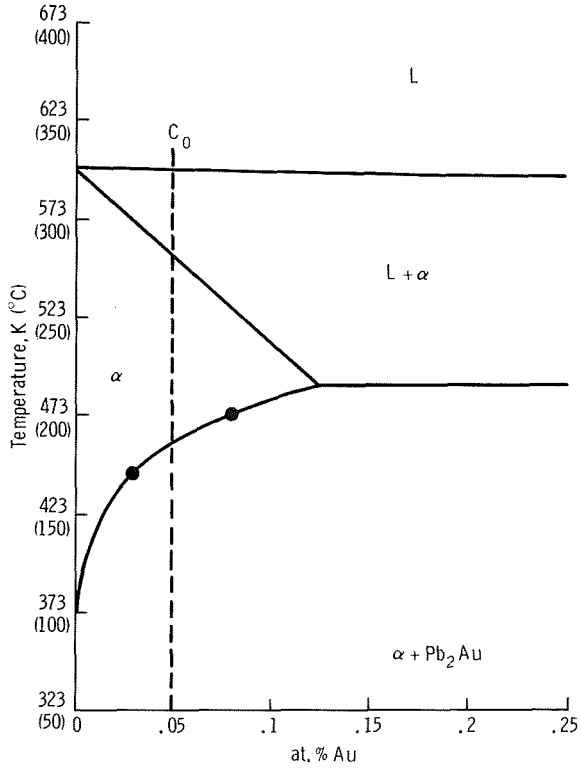

FIGURE 22-1.—The Pb-rich portion of the Pb-Au binary phase diagram, where C_0 is the initial Au concentration, α is a melting phase, and L is the liquidus phase. The curve was calculated on the basis of two experimental points in the relationship $C = A \exp[-(Q/RT)]$, where C is the Au concentration, A is a constant, Q is activation energy, R is the gas constant, and T is temperature (ref. 22-7).

TABLE 22-I.—Nuclear Data for Pb and Au

Property	*Element*	
	Pb	*Au*
Nuclear reaction	$^{208}Pb(n,\gamma)^{209}Pb$[a]	$^{197}Au(n,\gamma)^{198}Au$[a]
Abundance	52.3-percent ^{208}Pb	100-percent ^{197}Au
Thermal-neutron cross section, m^2 (b)	0.0005×10^{-28} (0.0005)	99×10^{-28} (99)
Radionuclide	^{209}Pb	^{198}Au
Type decay	β^-	β^-
β^-energy, MeV	0.64 (100 percent)	0.96 (96 percent)
Radionuclide half life, hr	3.3	64.8

[a] n = neutron; γ = gamma ray.

By calibrating the emulsion sensitivity to β^- radiation using samples of Pb containing known amounts of Au, quantitative analyses of the Au concentration in the experimental samples were made using a microphotometer to read the plates. This technique has been used successfully at ORNL for determination of tungsten and tantalum distributions in niobium (ref. 22-8).

3. It is believed that the Pb-Au system has large variations of surface tension with changes in composition. The variation of surface tension with temperature $d\sigma/dT$ is well known for Pb from the melting point to a temperature of approximately 1373 K (ref. 22-6, pp. 8 and 400). In fact, the value of $d\sigma/dT$ ranges from -0.0062 to -0.0120 $\mu J/cm^2$ K (-0.062 to -0.120 erg/cm^2 K). The variation of surface tension with composition $d\sigma/dc$ has not been determined for the Pb-Au system. However, a similar system, tin-copper, has been studied (ref. 22-6, p. 258). For tin-copper, a slight negative deviation from a linear relationship was found. Thus, assuming a linear relationship between the surface tension of Pb (39.5 $\mu J/cm^2$ (395 ergs/cm^2)) and Au (112.5 $\mu J/cm^2$ (1125 ergs/cm^2)) at a common temperature of 1373 K, the value of $d\sigma/dc$ can be estimated as approximately 0.73 $\mu J/cm^2$ at.% (7.3 ergs/cm^2 at.% The interfacial energies for the alloy-graphite, lead-graphite, alloy-mild steel, and lead-mild steel systems that were used in the experiment are not known.

EXPERIMENTAL DESIGN

A schematic representation of the specimen arrangement in the multipurpose electric furnace is shown in figure 22-2. Because of longitudinal heat flow in the furnace during operation, the specimens melted from left to right with reference to the representation (fig. 22-2) and solidified in the reverse direction; as is shown, six flight specimens were used in the Apollo-Soyuz experiment. The furnace and the cartridges that contained the specimen ampoules were constructed so that each ampoule would experience minimum temperature gradients. Two of the three flight cartridges contained specimens loaded in graphite containers. The two cartridges were identical except for the location of the Pb-0.05 at.% Au alloy. In one cartridge (flight cartridge 2), the alloy was located on the hot end and thus melted first; in the other cartridge (flight cartridge 3), the alloy was located on the reverse end of the specimen and thus melted last and solidified first. This arrangement was designed to determine whether melting or solidification affected the Au concentration

profile. Flight cartridge 1 (fig. 22-2) contained two specimens in mild steel capsules with the Pb-Au alloy alined so that it melted first. An identical specimen arrangement was used for ground-based tests to provide comparison between the different transport mechanisms in liquid metals processed in space and in a unit gravity environment.

Dimensions of the actual specimens are shown in figure 22-3. The 3-mm-thick Pb-0.05 at.%Au alloy disk was cold-pressure welded to the pure Pb. It should be noted that the total diffusion distance available was approximately 3 cm.

Ampoules (mild steel and stainless steel lined with graphite) used for the specimens described in this report are shown in figures 22-4 and 22-5, respectively. In the graphite-lined container, quartz cloth disks were placed at each end to provide padding for normal handling movements and to adjust the void space in the ampoule. Originally, it was anticipated that specimens attaining the 923-K temperature would be in the liquid state approximately 2 hours and that specimens heated to a temperature of 723 K would be molten approximately 1 hour. Liquid diffusion data for Au in Pb are not available. However, by using the results from the Skylab Zn self-diffusion experiment (ref. 22-5, p. 440), it was possible to estimate some diffusion distances for this experiment. Figure 22-6 contains the calculated Au concentration-distance profiles for a geometry consisting of a 3-mm-thick disk of Pb-0.05 at.% Au alloy bonded to pure Pb to form a cylindrical specimen 3 cm long. These concentration-distance profiles were calculated using the solution for an extended source of limited extent from reference 22-9 (pp. 11 to 14). The source width h was 3 mm; the diffusion temperatures were 673 and 923 K for figures 22-6(a) and 22-6(b), respectively. The diffusivity value D is calculated from the Zn self-diffusion

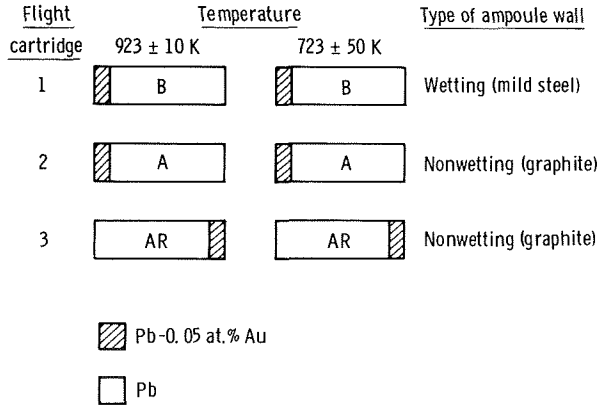

FIGURE 22-2.—Schematic arrangement of specimens in multipurpose furnace. (Letters indicate specimen notation used in this report.)

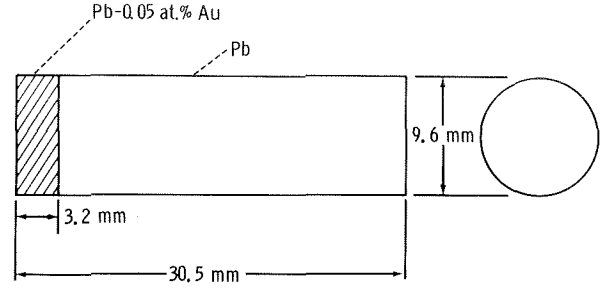

FIGURE 22-3.—Dimensions of MA-041 specimen.

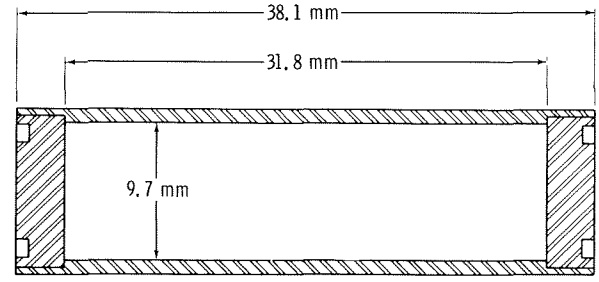

FIGURE 22-4.—Mild steel (type 1015) ampoule assembly for type B specimen capsules.

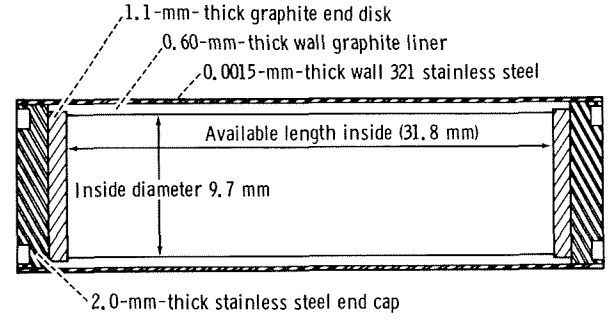
1.1-mm-thick graphite end disk
0.60-mm-thick wall graphite liner
0.0015-mm-thick wall 321 stainless steel
Available length inside (31.8 mm)
Inside diameter 9.7 mm
2.0-mm-thick stainless steel end cap

FIGURE 22-5.—Graphite-lined stainless steel assembly for type A and AR specimens.

results of reference 22-5 (p. 440). Figure 22-6(a), in which an effective diffusion temperature of 673 K is assumed, shows that diffusion distances of approximately 1.5 cm would be achieved in 1 hour. Figure 22-6(b), calculated for 923 K, indicates that a diffusion distance of 2.7 cm would be expected within 2 hours at the diffusion temperature. Assuming an initial concentration of Au in Pb C_0 of 500 atomic parts per million (at. p/m), the Au concentration in the pellet would be reduced to 215 and 130 at. p/m at 673 and 923 K, respectively. These estimated distances and concentrations were within the limits of the experimental design capabilities.

FURNACE THERMAL CHARACTERISTICS AND OTHER IMPORTANT EXPERIMENTAL PARAMETERS

Temperature-time data monitored on the Apollo-Soyuz mission were obtained by measurements made on the heat-leveler block of the multipurpose furnace (fig. 22-7). Because the furnace operation during flight was longer than planned, a postflight ground-based test (GBT) was performed to duplicate the space-flight furnace operation. The temperature-time curves are shown in figure 22-8. Table 22-II contains the heating and cooling rates for both ground based (GB) and space-flight (SF) specimens at a temperature of 600 K. The approximate solidification rates for both GB and SF specimens were determined by dividing the change in temperature per unit time by the change in temperature per unit length. The results are as follows.

1. 2.5 cm/min for the 923-K-temperature-zone GB specimens
2. 9.0 cm/min for the 723-K-temperature-zone GB specimens
3. 2.5 cm/min for the 923-K-temperature-zone SF specimens
4. 6.0 cm/min for the 723-K-temperature-zone SF specimens

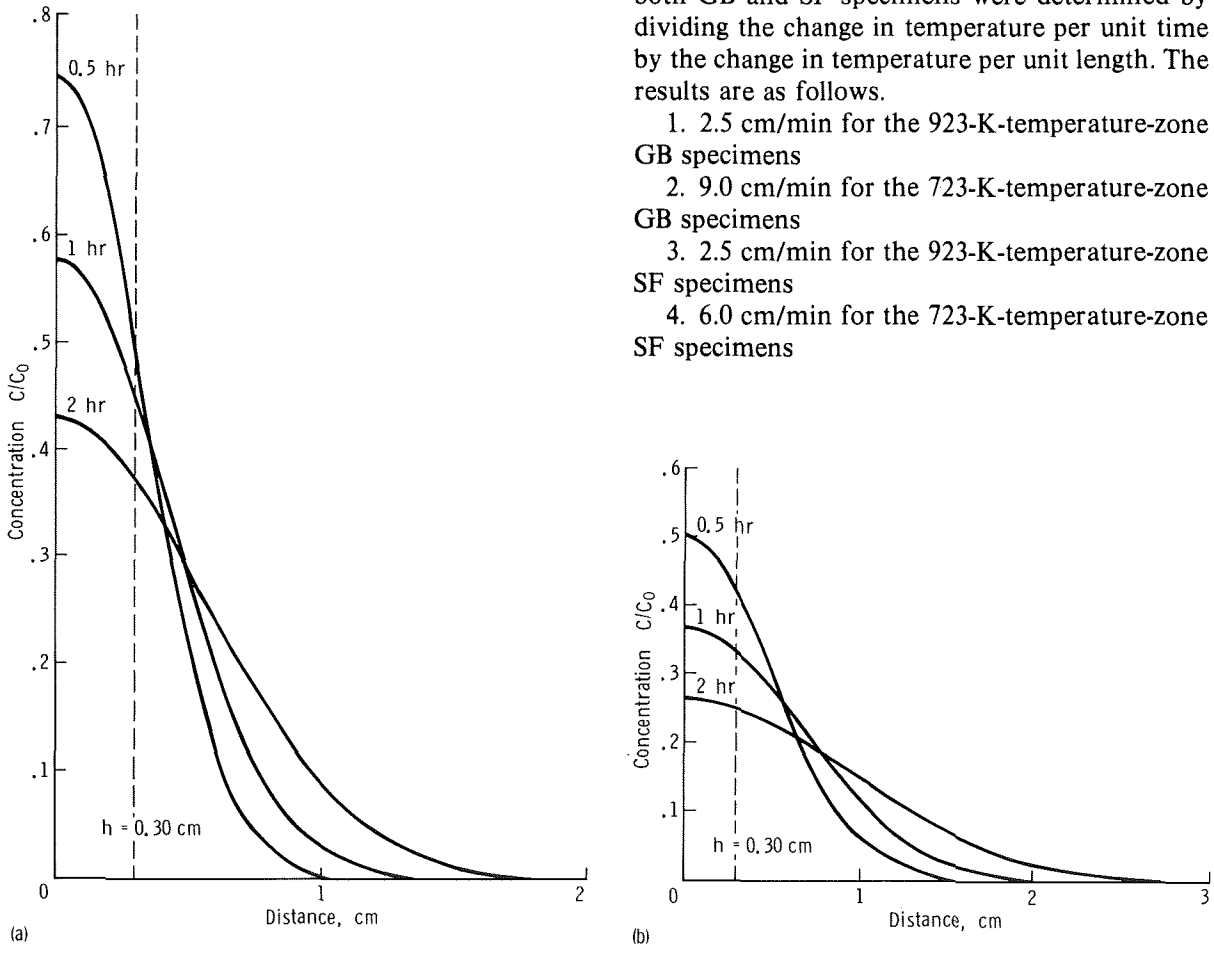

FIGURE 22-6.—Concentration-distance profiles calculated using the solution for an extended source of limited extent (ref. 22-9), where the source width $h = 3$ mm, T is the diffusion temperature, and D is the diffusivity value calculated from Zn self-diffusion data (ref. 22-5, p. 440). (a) $D = 1.93 \times 10^{-5}$ cm^2/sec; $T = 673$ K (400° C). (b) $D = 5.50 \times 10^{-5}$ cm^2/sec; $T = 923$ K (650° C).

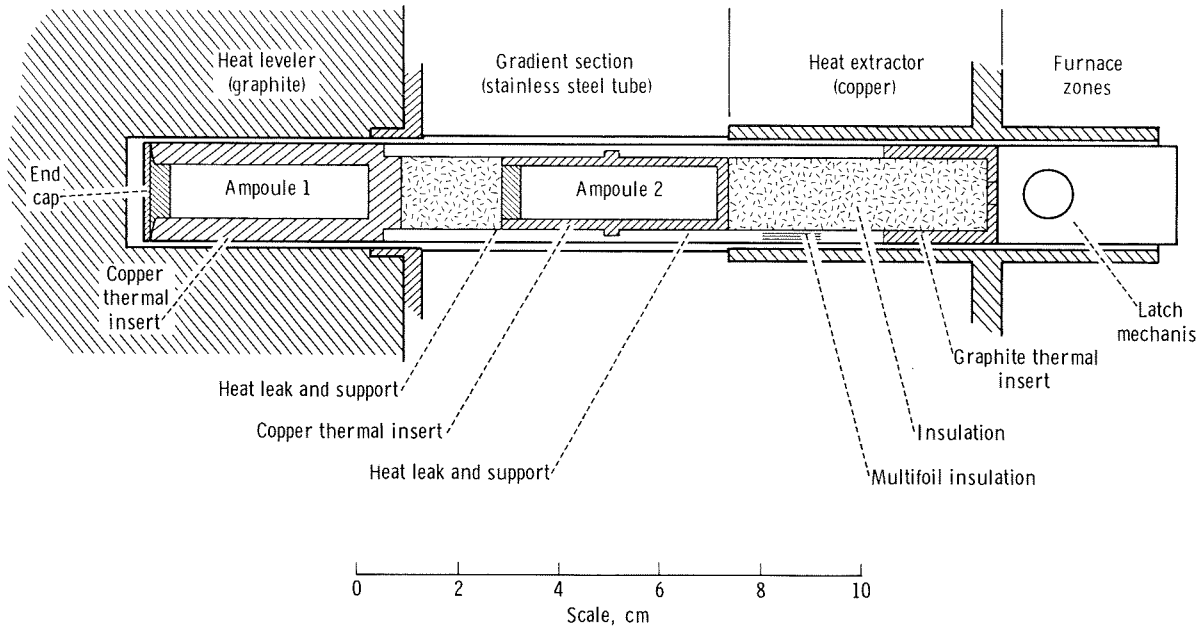

FIGURE 22-7.—Diagram of MA-041 advanced flight cartridge.

It was determined from the flight analyses that ampoules A and B were in the liquid phase for 268 and 82 minutes, respectively. In the GBT-25 experiment, the specimens remained in the liquid phase 226 and 77 minutes for ampoules A and B, respectively.[1] Additional experimental values that must be considered in the experimental analyses are as follows.

1. The relative density difference $\Delta\rho/\rho$ between the Pb-Au alloy and the pure Pb was 1.76×10^{-4}
2. The equilibrium distribution coefficient K of Au in Pb is nearly 0.3.
3. Cooling rates dT/dt, where t is time, were in the range of 1 to 10 K/min.
4. The temperature gradient G, which was purposely kept small to maintain a constant-temperature diffusion rate, was in the range of 0.4 to 2.0 K/cm.
5. The calculated solidification velocity V was in the range of 2.5 to 9 cm/min.

The average acceleration of the SF specimens during the experiment was less than 0.0981 cm/sec^2. Maximum acceleration, which was caused by firing of the reaction control system thrusters, was less than 5.886 cm/sec^2 for time periods of 15 milliseconds.

SAMPLE PREPARATION FOR POSTMISSION ANALYSES

Sample numbers for each specimen used in both the ground-based and space-flight experiments are shown in table 22-III. The samples are coded as follows. The "A" suffix indicates specimens in graphite-lined stainless steel containers with the Pb-0.05 at.% Au alloy located at the hot end of the temperature zone. The "AR" suffix indicates specimens in graphite-lined stainless steel containers with the Pb-Au alloy located away from the hot end (i.e., the "reverse" end) of the temperature zone. The "B" suffix indicates specimens in unlined mild steel containers with the Pb-Au alloy located at the temperature-zone hot end,

[1] W. S. Key, Technical Letter ASD-EP 44-22716, Teledyne Brown Engineering, December 16, 1975.

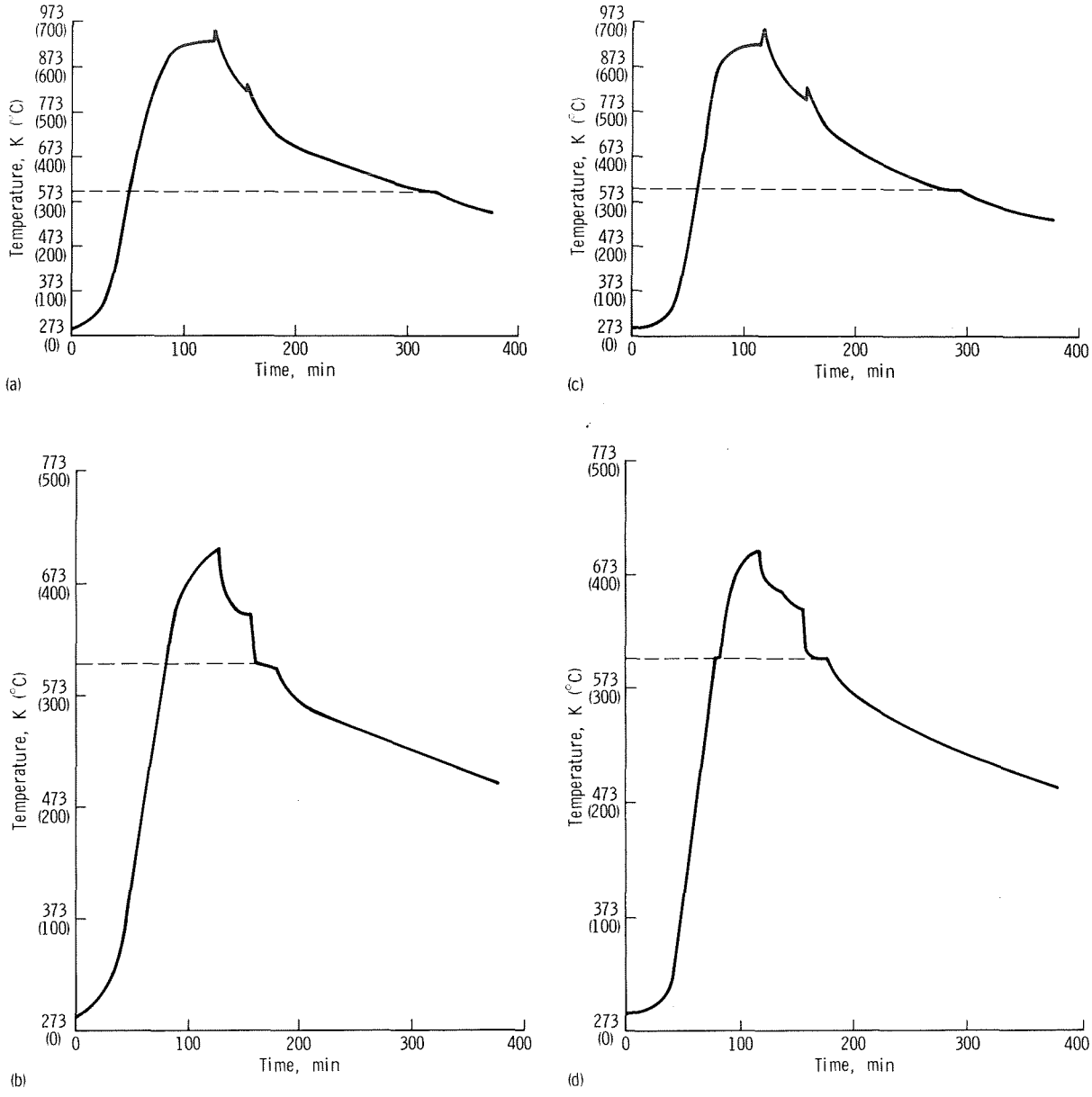

FIGURE 22-8.—Temperature-time history for MA-041 specimens. The dashed line is at 600 K, the melting point of Pb. (a) 923-K SF specimens. (b) 723-K SF specimens. (c) 923-K GB specimens. (d) 723-K GB specimens.

which was the only alloy location in mild steel containers. (See fig. 22-2.)

After completion of the melting experiments (both ground based and space flight), the specimens were returned to the laboratory for sectioning and subsequent analysis. After removal from the nonwetting ampoules, the A and AR specimens were potted in epoxy for longitudinal sectioning. The wetting-type, mild steel ampoules containing the B alloy specimens were mounted in epoxy resin and sectioned longitudinally together with the specimens. The epoxy potting material was then dissolved and each specimen, together

TABLE 22-II.—Heating and Cooling Rates for GB and SF Specimen Ampoules

Characteristic	*Temperature history*			
	GB specimens[a]		*SF specimens*[b]	
	923-K zone	*723-K zone*	*923-K zone*	*723-K zone*
Heating rate at 600 K, K/min	7	2	11	4
Cooling rate at 600 K, K/min	1	10	1	5

[a]Heating and cooling rates based on the slopes of the temperature curves at 600 K at nodes 312 and 322 for GBT-25.
[b]Heating and cooling rates based on the slopes of the temperature curves at 600 K at nodes 312 and 322 for the SF ampoules.

TABLE 22-III.—Sample Nomenclature and Location for MA-041 Specimens[a]

Container type	*Specimen number and location*	
	923-K zone	*723-K zone*
SF specimens		
Graphite	11-A	21-A
Graphite	13-AR	17-AR
Mild steel	12-B	21-B
GB specimens		
Graphite	17-A	14-A
Graphite	11-AR	20-AR
Mild steel	13-B	15-B

[a]Schematic arrangement of specimens is shown in figure 22-2.

with seven Pb-Au alloy calibration disks, was remounted in a 5-cm-diameter epoxy mount and metallographically polished.

The specimens were irradiated in the Bulk Shielding Reactor for 4 hours in essentially a pure thermal flux of 1.2×10^{12} neutrons sec^{-1} cm^{-2}. During irradiation, both ^{209}Pb and ^{198}Au are formed. The activity of interest is ^{198}Au, which decays by the emission of 0.960-MeV beta particles and has a half-life of 64.8 hours. The ^{209}Pb formed during the irradiation is essentially nonexistent after approximately 24 hours, because the thermal-neutron cross section for forming ^{209}Pb from ^{208}Pb is small and the ^{209}Pb half-life is only 3.3 hours. After the radioactive nuclides decayed for 24 to 30 hours, autoradiographs of the specimens were made.

Autoradiographs were made in complete darkness in the same darkroom in which the film was developed after exposure. The polished face of the mount was placed face down on Kodak industrial type R X-ray film, an ultra-fine-grain, single-emulsion film. Exposures were made for durations of 8, 16, 32, 64, 128, and 256 minutes. The film is exposed to β^- emission from the Au in the Pb. Because the range of the 0.960-MeV β^- in Pb is approximately 0.4 mm, only the Au concentration in this layer thickness is detected.

Originally, seven Pb-Au standards of 0, 20, 52, 91, 217, 277, and 393 at. p/m Au were used. The arrangement of the standards and the specimen for the first irradiation is shown in figure 22-9. Beta scattering from the standards distorted the Au concentration profiles in both the GB and the SF specimens in the area of the specimens adjacent to the standards. In addition, beta scattering influenced the radiation values obtained for each standard. Thus, to eliminate the beta-scattering problem, two epoxy mounts were necessary; one contained the Pb-Au standards and one contained the specimen. This arrangement is shown in figure 22-10. The 277 and 393 at. p/m Au standards were not used because the original irradiation verified that all Au concentrations in the specimens were below these values.

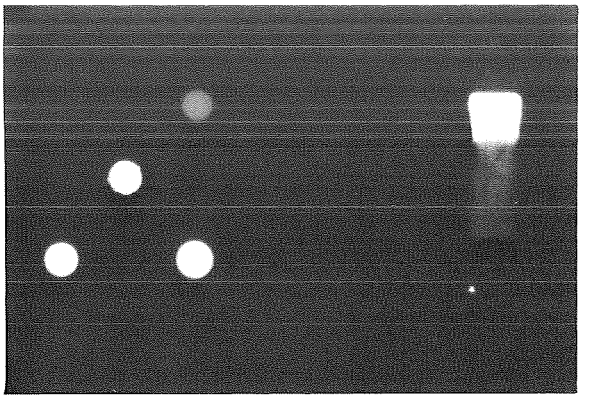

FIGURE 22-10.—This print, taken from a deliberately overexposed autoradiograph, shows the relative locations of the Pb-Au standards (disks) and the specimen during autoradiography. Light areas indicate Au activity.

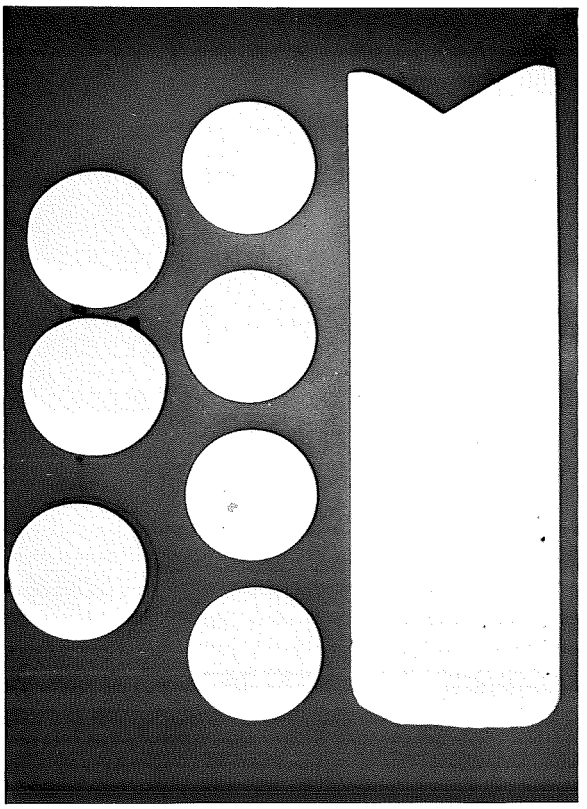

FIGURE 22-9.—Macrograph of the longitudinally cut surface of SF specimen 17-AR and seven Pb-Au standards mounted in epoxy resin.

EXAMINATION OF SPECIMEN EXTERIORS AND LONGITUDINAL SECTIONS

A visual examination of both the GB and SF specimens after removal from the ampoules revealed no evidence of oxidation.

Ground-Based Specimens

The exterior surfaces of the A and AR GB specimens are shown in figures 22-11 to 22-16. A side view of GB specimens 17-A and 14-A, which were mounted vertically in the multipurpose electric furnace and were located in the 923- and 723-K temperature zones, respectively, is shown in figure 22-11. The samples melted from the top to the bottom (fig. 22-11) and, upon cooling, solidified in the reverse direction. The original bond interface of the Pb-Au disks can still be discerned at the top of each specimen. In addition, both specimens show the expected sharp corners at the base.

A bottom view of specimens 17-A and 14-A is shown in figure 22-12. This figure shows the sharp corners as well as ripples due to the quartz spacer cloth. Figure 22-13 is a top view of GB specimen 17-A. Evidence of a solidification pipe, which was not evident for specimen 14-A, can be seen.

A side view of GB specimens 11-AR and 20-AR is shown in figure 22-14. Like the previous

specimens (17-A and 14-A), specimens 11-AR and 20-AR were mounted vertically in the multipurpose electric furnace and were located in the 923- and 723-K temperature zones, respectively. However, the 11-AR and 20-AR Pb-Au alloy disks were located at the bottom and thus melted last and solidified first. Again, the original bond interface and the square corners can be seen at the bottom of the specimens. The top view of specimens 11-AR and 20-AR is shown in figure 22-15. Evidence of a solidification pipe can be seen for specimen 11-AR but not for 20-AR. A bottom view of the two specimens can be seen in figure 22-16. Characteristics to note are the ripples due to the quartz spacer cloth and the Pb-Au bond interface.

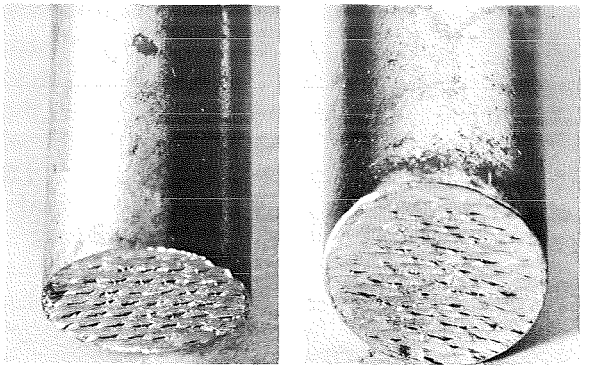

FIGURE 22-12.—Photograph of the lower ends of GB specimens 17-A (left) and 14-A (right).

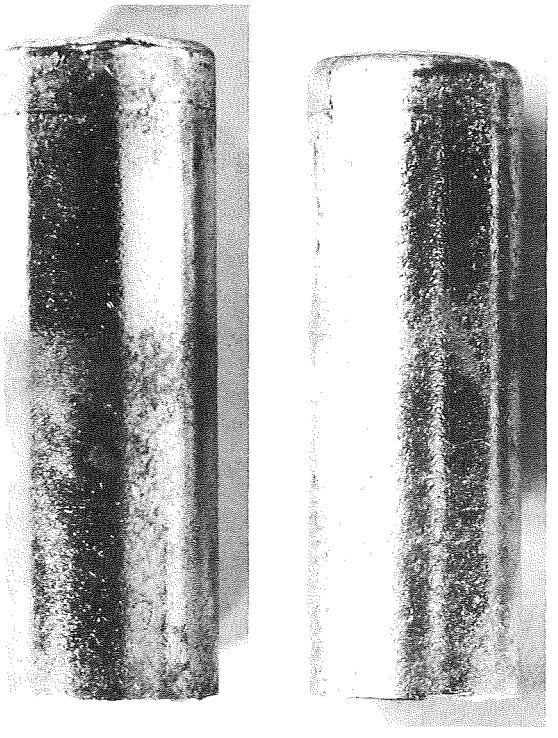

FIGURE 22-11.—Photograph of GB specimens 17-A (left) and 14-A (right), which were located in the 923- and 723-K temperature zones, respectively, of the multipurpose furnace. The specimens are approximately 1 cm in diameter.

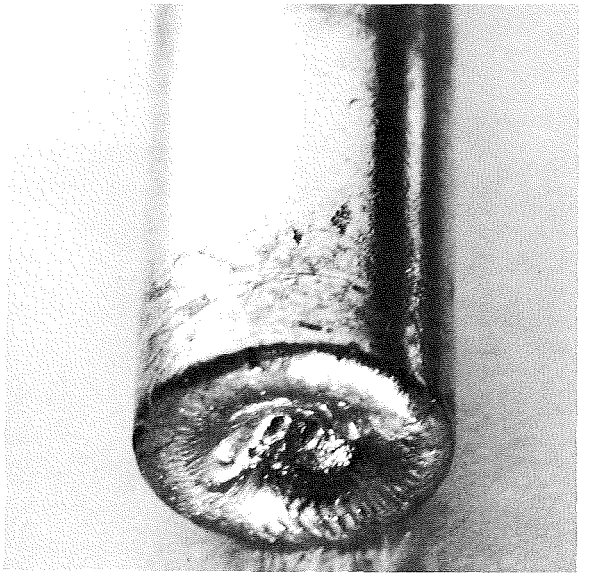

FIGURE 22-13.—Photograph of the upper end of GB specimen 17-A.

Macrographs of the metallographically polished, longitudinally sectioned surfaces of GB specimens 17-A, 11-AR, 14-A, and 20-AR are shown in figures 22-17 and 22-18. The solidification pipe is clearly seen for the two 923-K specimens (figs. 22-17(a) and 22-17(b)). The 723-K

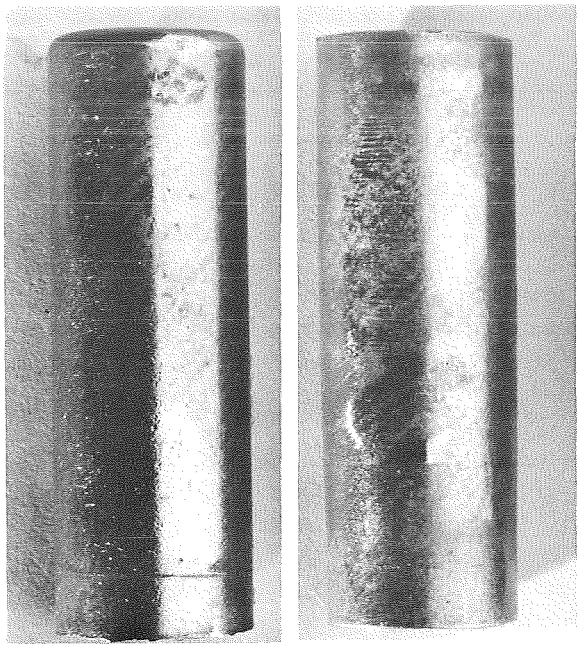

FIGURE 22-14.—Photograph of GB specimens 11-AR (left) and 20-AR (right), which were located in the 923- and 723-K temperature zones, respectively, of the multipurpose furnace.

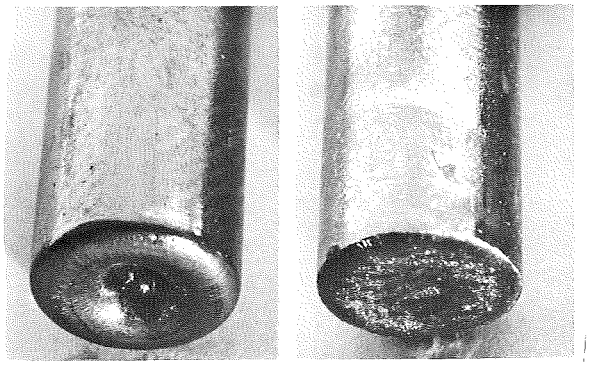

FIGURE 22-15.—Photograph of the upper ends of GB specimens 11-AR (left) and 20-AR (right).

specimens (figs. 22-18(a) and 22-18(b)) have square corners and reveal no evidence of solidification pipes.

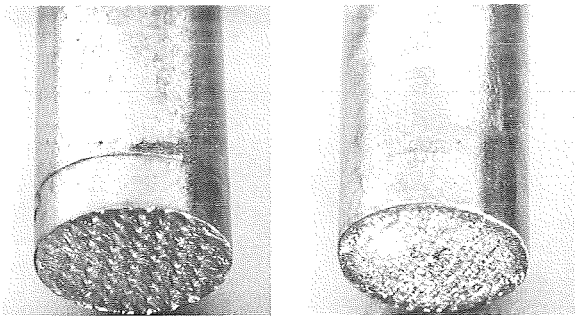

FIGURE 22-16.—Photograph of the lower end of GB specimens 11-AR (left) and 20-AR (right).

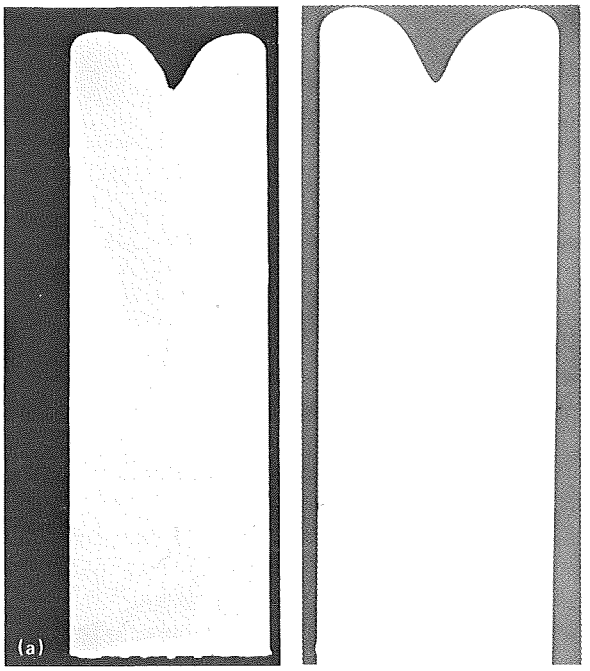

FIGURE 22-17.—Macrographs of metallographically polished, longitudinally sectioned surfaces of 923-K GB specimens. The specimens solidified from bottom to top in a nonwetting ampoule. (a) Specimen 17-A; Pb-Au alloy disk originally located at top. (b) Specimen 11-AR; Pb-Au alloy disk originally located at bottom.

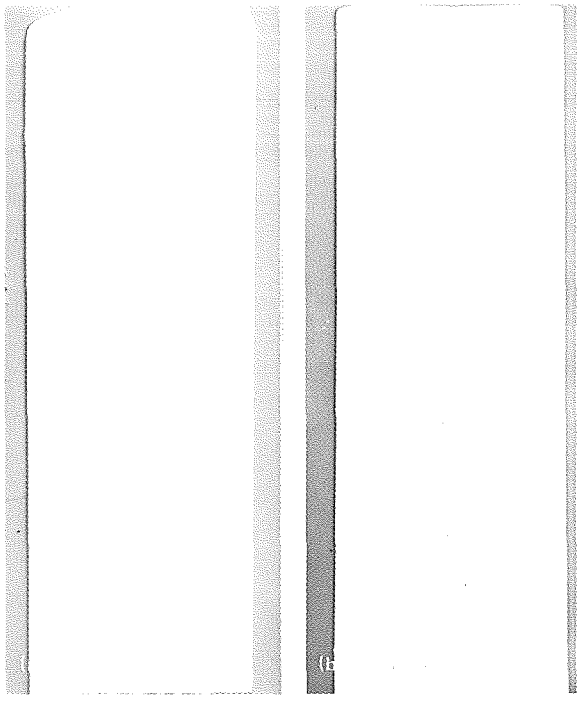

FIGURE 22-18.—Macrographs of metallographically polished, longitudinally sectioned surfaces of 723-K GB specimens. The specimens solidified from bottom to top in a nonwetting ampoule. (a) Specimen 14-A; Pb-Au alloy disk originally located at top. (b) Specimen 20-AR; Pb-Au alloy disk originally located at bottom.

Space-Flight Specimens

The exterior surfaces of the A and AR SF specimens are shown in figures 22-19 to 22-24. A side view of SF specimens 11-A and 21-A is shown in figure 22-19. Cellular structure at the top is clearly evident for specimen 11-A, which was located in the 923-K temperature zone, but not as evident for the 723-K zone specimen (21-A). The specimens melted from the top to the bottom (fig. 22-19) and solidified in the reverse direction. A bottom view of specimens 11-A and 21-A is shown in figure 22-20. The SF samples have rounded edges and no evidence of ripple marks from the quartz spacer cloth. Figure 22-21 is a top view of specimen 11-A showing the Pb-Au alloy disk region. The cellular structure and the Pb-Au bond interface are clearly distinguishable.

A side view of SF specimens 13-AR and 17-AR is shown in figure 22-22. Again, one can see the cellular structure for the 923-K-temperature-zone specimen (13-AR) in the Au-rich region at the bottom. This structure is not evident for the 723-K-zone specimen (17-AR). A top view (opposite from the Pb-Au alloy disk) in figure 22-23 reveals evidence of solidification pipes for both specimens. The Pb-Au alloy region for specimens 13-AR and 17-AR is shown in figure 22-24; this end of the specimen melted last and solidified first. The cellular structure and the Pb-Au bond interface can be seen for both specimens.

Macrographs of the metallographically polished, longitudinally sectioned surfaces of the SF specimens are shown in figures 22-25 and 22-26. The macrograph for SF specimen 11-A (fig. 22-25(a)) shows the expected rounded corners. This specimen was located in the 923-K temperature zone. The AR SF specimen from the same temperature zone (fig. 22-25(b)) also has rounded corners. In addition, a large solidification

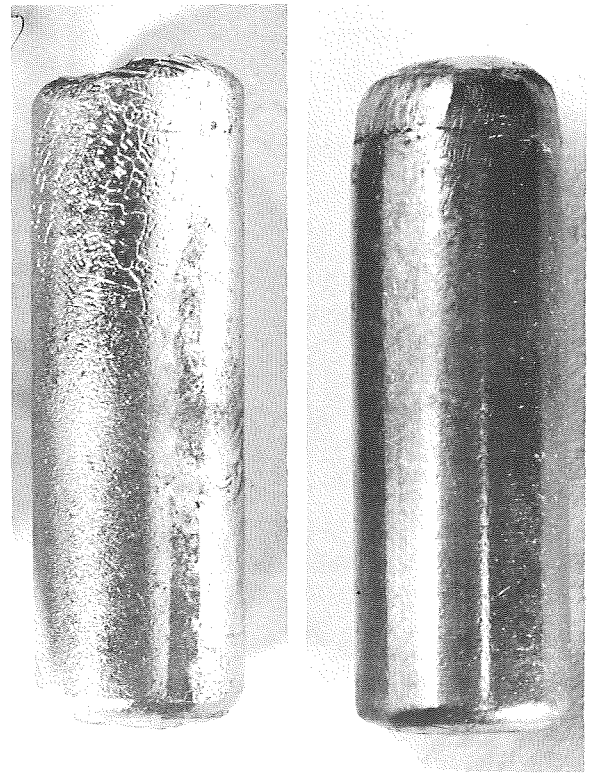

FIGURE 22-19.—Photograph of SF specimens 11-A (left) and 21-A (right), which were located in the 923- and 723-K temperature zones, respectively, of the multipurpose furnace.

pipe was formed at the top of the specimen. Macrographs of the polished longitudinal sections of the 723-K-temperature-zone A and AR SF specimens are shown in figures 22-26(a) and 22-26(b), respectively. These specimens have characteristics similar to those described for the 923-K-zone SF specimens.

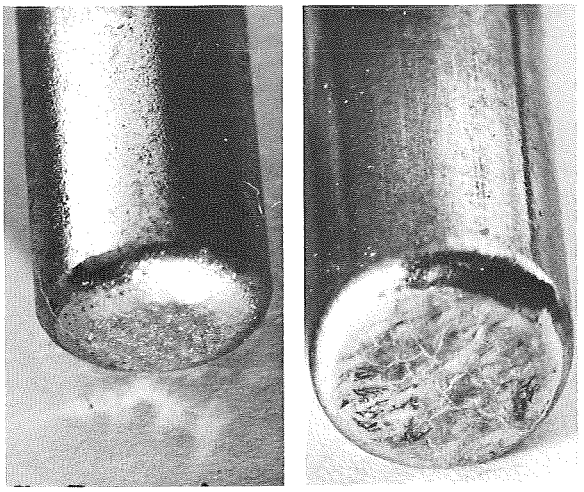

FIGURE 22-20.—Photograph of the lower end of SF specimens 11-A (left) and 21-A (right).

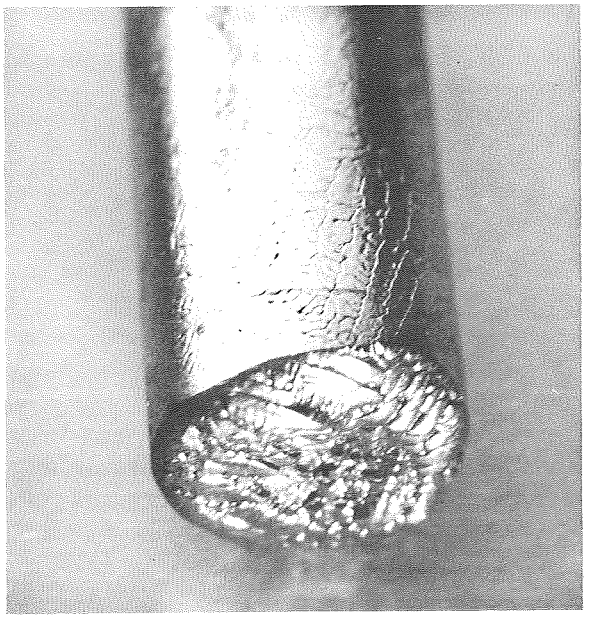

FIGURE 22-21.—Photograph of the upper end of SF specimen 11-A.

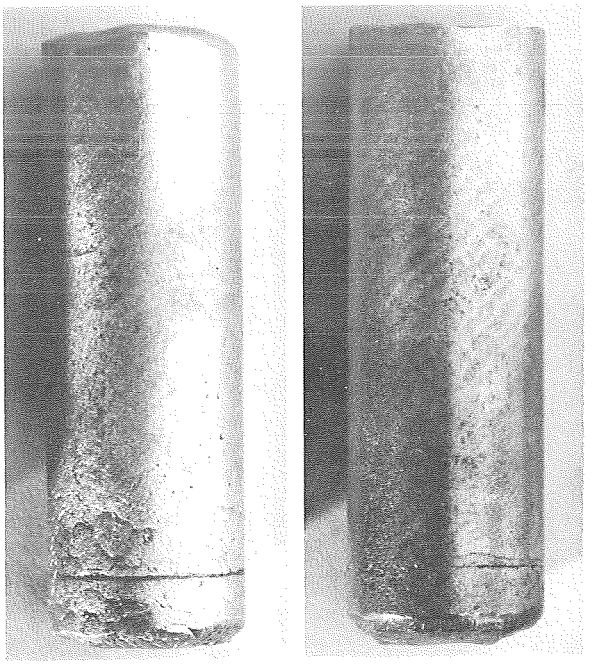

FIGURE 22-22.—Photograph of SF specimens 13-AR (left) and 17-AR (right), which were located in the 923- and 723-K temperature zones, respectively, of the multipurpose furnace.

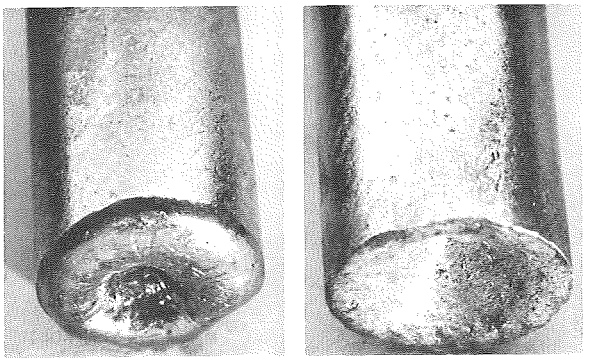

FIGURE 22-23.—Photograph of upper end of SF specimens 13-AR (left) and 17-AR (right).

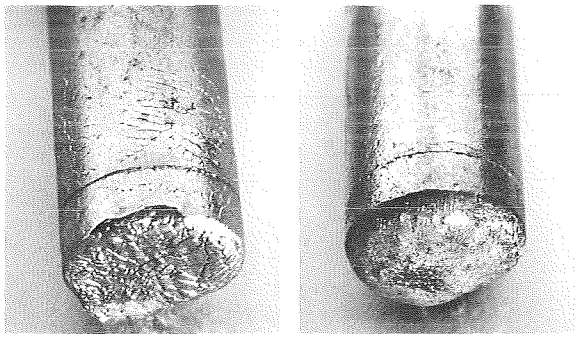

FIGURE 22-24.—Photograph of lower end of SF specimens 13-AR (left) and 17-AR (right).

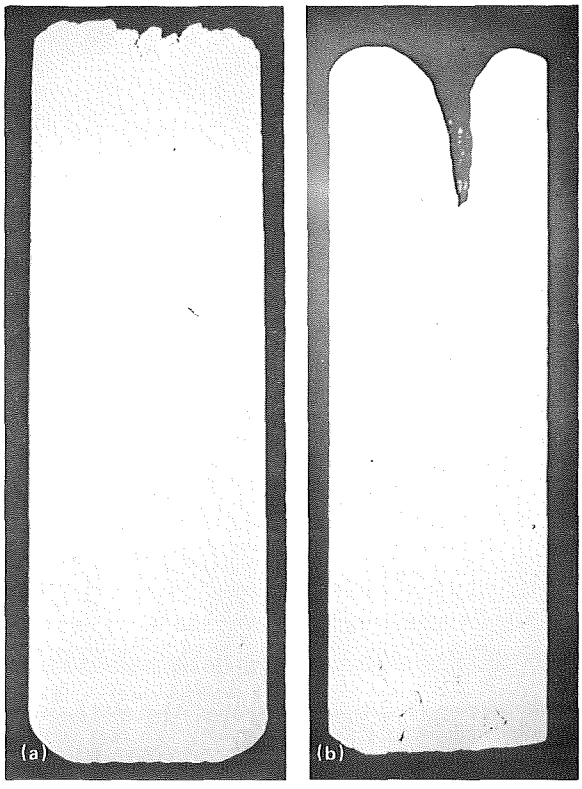

FIGURE 22-25.—Macrographs of metallographically polished, longitudinally sectioned surfaces of 923-K SF specimens. The specimens solidified from bottom to top in a nonwetting ampoule. (a) Specimen 11-A; Pb-Au alloy disk originally located at top. (b) Specimen 13-AR; Pb-Au alloy disk originally located at bottom.

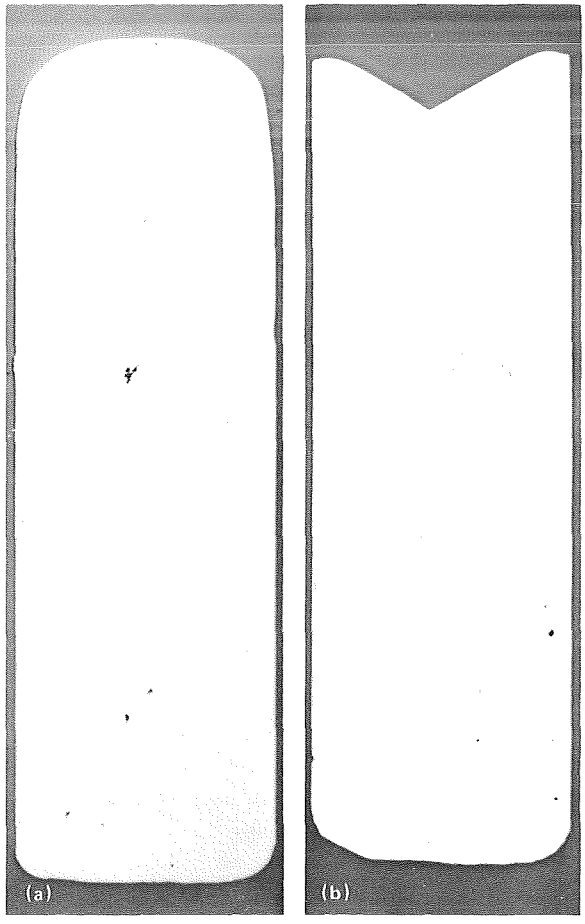

FIGURE 22-26.—Macrographs of metallographically polished, longitudinally sectioned surfaces of 723-K SF specimens. The specimens solidified from bottom to top in a nonwetting ampoule. (a) Specimen 21-A; Pb-Au alloy disk originally located at top. (b) Specimen 17-AR; Pb-Au alloy disk originally located at bottom.

DIFFUSION ANALYSIS

If no convective stirring effects were present during the period in which the samples were molten, a normal diffusion concentration-distance profile would be expected. As shown in figures 22-27(a) to 22-27(d), the right-hand portion of the Au-concentration profiles for the central slices of the SF specimens resemble profiles that would

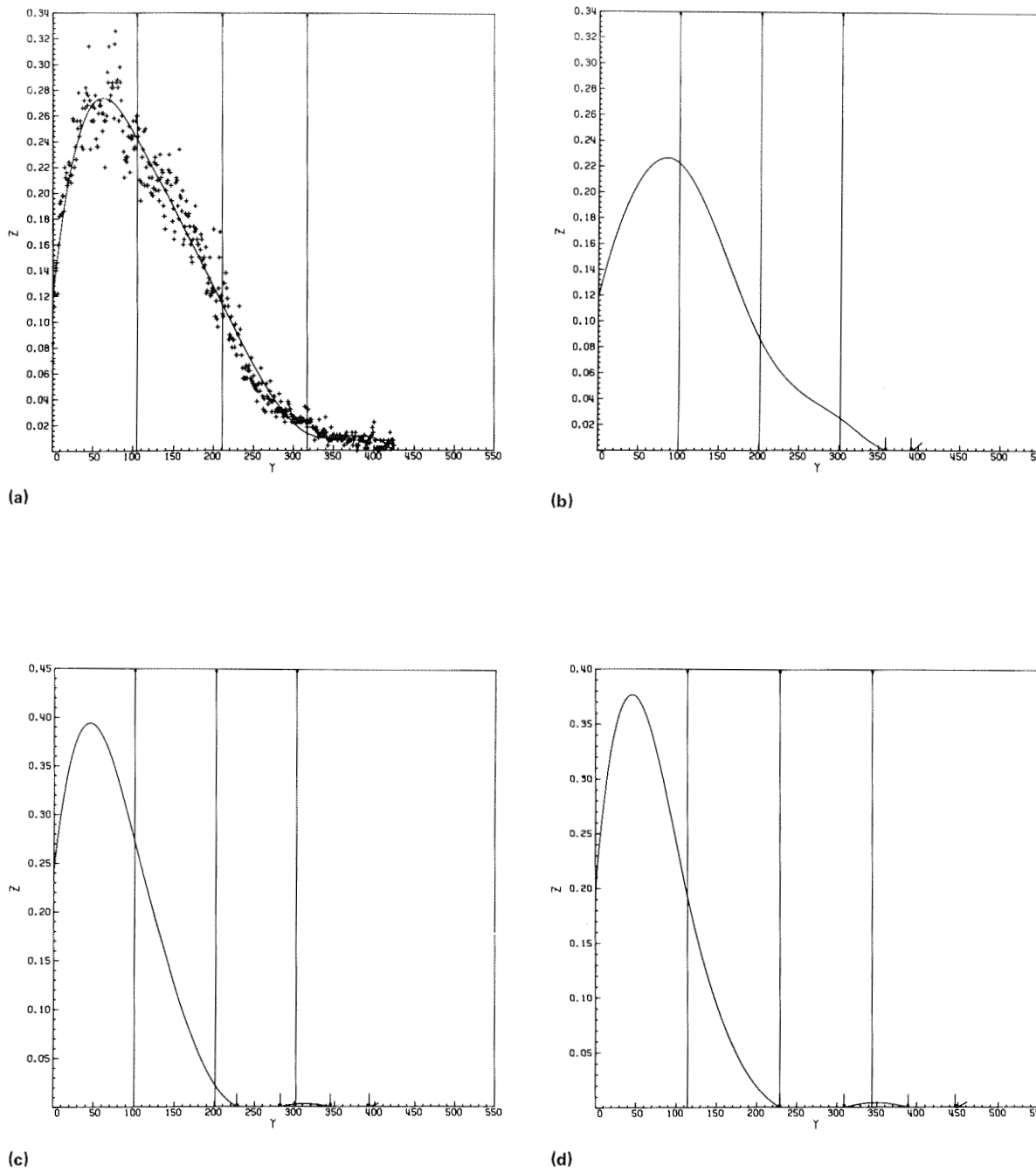

FIGURE 22-27.—Computer printouts giving central axial Au-concentration profiles for SF specimens. The ordinate Z represents the percentage of Au with respect to the initial concentration of 500 at. p/m. The abscissa Y corresponds to a specific column number that can be converted to distance in millimeters by dividing by 14.5 (i.e., 14.5 columns/mm). (a) Specimen 11-A; all data points (approximately 420) are shown. (b) Specimen 13-AR. (c) Specimen 21-A. (d) Specimen 17-AR.

result essentially from diffusion. Thus, an attempt was made to calculate the diffusion constant D_0 and the activation energy A for the liquid diffusion of Au in Pb by assuming the following definition of diffusion coefficient D.

$$D = D_0 \exp\left(-\frac{A}{RT}\right) \tag{22-1}$$

where R is the gas constant (8.314 J/mol K (1.987 cal/mol K)) and T is temperature. Because of a malfunction in the helium quenching process, the SF specimens stayed molten longer than was initially anticipated. As shown in figures 22-8(a) to 22-8(d), the temperature was not constant but decreased at a slow rate during the cooldown process. Thus, the diffusion coefficients would be expected to have temperature dependency. To solve this problem, according to Crank (ref. 22-9, p.9), one uses the solutions of the diffusion differential equation

$$\frac{\delta C}{\delta T^*} = \frac{\delta^2 C}{\delta x^2} \tag{22-2}$$

where C is concentration, x is diffusion distance, and T^* is defined as

$$T^* = \int_0^t D(t')dt' \tag{22-3}$$

where t is time. Substituting equation (22-1) into equation (22-3) gives

$$T^* = D_0 \int_0^t \exp\left(-\frac{A}{RT(t')}\right) dt' \tag{22-4}$$

Solving equation (22-1) with the boundary conditions (1) extended source of length h and constant concentration C_0 and (2) finite specimen length ℓ, one obtains (ref. 22-9, p.15)

$$\frac{C}{C_0} = \frac{1}{2} \sum_{n=-\infty}^{\infty} \left[\operatorname{erf} \frac{h + 2n\ell - x}{2\sqrt{T^*}} + \operatorname{erf} \frac{h - 2n\ell + x}{2\sqrt{T^*}} \right] \tag{22-5}$$

where integer counter $n \geq -\infty$. It is evident that T^* (eq. (22-4)) is a function of the temperature-time history of the specimens. Because the specimens in this experiment were located in two temperature zones, there are two temperature-time histories and consequently two T^* values, as follows.

$$T_1^* = D_0 \int_0^{t_1} \exp\left(-\frac{A}{RT_1(t')}\right) dt' \tag{22-6}$$

and

$$T_2^* = D_0 \int_0^{t_2} \exp\left(-\frac{A}{RT_2(t')}\right) dt' \tag{22-7}$$

One method of determining the activation energy is to define a function $G(A)$ as follows.

$$G(A) = \frac{\int_0^{t_1} \exp\left(-\frac{A}{RT_1(t')}\right) dt'}{\int_0^{t_2} \exp\left(-\frac{A}{RT_2(t')}\right) dt'} = \frac{T_1^*}{T_2^*} \tag{22-8}$$

Using this function, the quotient of the experimentally determined values of T_1^* divided by T_2^* defines the actual value of $G(A)$. Using the calculated values for the function $G(A)$ shown in figure 22-28, one should be able to determine the activation energy for the Pb-Au system.

Equation (22-5) was used to obtain the best fit for the concentration profiles for the central slices of the four SF specimens, neglecting the six lowest concentration values shown on the experimental curves. An example of such a fit for SF specimen 13-AR is shown in figure 22-29. The T^* values obtained for the four SF specimens are shown in table 22-IV. Taking the average value for the two temperature zones and using equation (22-8), a value of 2.12 is obtained for $G(A)$. Figure 22-28 indicates that the corresponding activation energy would be extremely small (or negative). This low

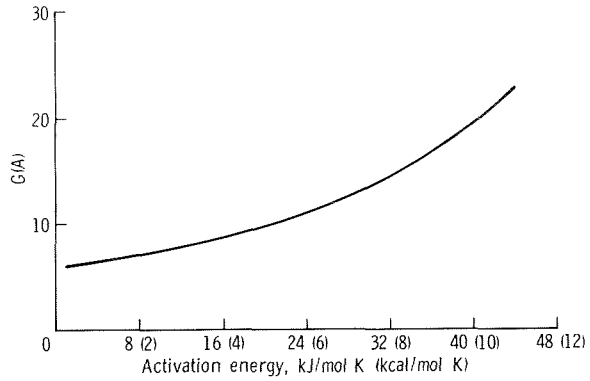

FIGURE 22-28.—Plot of equation (22-8) for the two temperature-time histories of Experiment MA-041 and different activation energies.

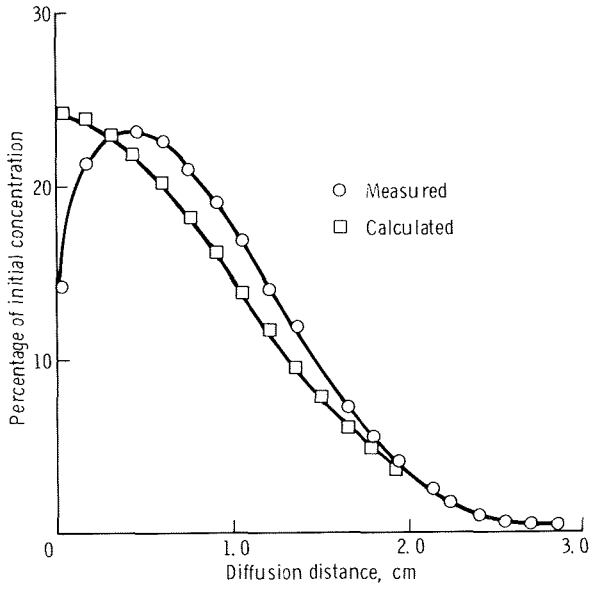

FIGURE 22-29.—Comparison of measured and calculated diffusion profiles for SF specimen 13-AR. The calculated curve was plotted using equation (22-5).

value does not appear reasonable because the reported activation energies for most liquid diffusion systems are greater than 4 kJ/mol K (>1 kcal/mol K) (ref. 22-10, p. 316).

To clarify the discrepancy, the Zn self-diffusion data taken from the Skylab experiment (ref. 22-5, p. 440) were used in conjunction with the two temperature-time histories for this experiment to calculate concentration profiles. The calculated concentration profiles, using a D_0 value of 9.17×10^{-4} and an activation energy of 21 589 J/mol K (5160 cal/mol K), are compared with the experimental concentration profiles for SF specimens 11-A and 21-A in figures 22-30(a) and 22-30(b), respectively. Curves 1 and 2 in figures 22-30(a) and 22-30(b) represent the experimental values. Curve 1 represents the actual Au concentration in the central slice. Because of the increased Au concentration in the central region of the SF specimens, it was believed that the true diffusion process would be better represented by a curve adjusted to show no Au increase. Thus, curve 2 was obtained by adjusting the experimental values by the amount of Au-concentration increase in the central region. It is evident that the calculated values for the 923-K SF specimen (fig. 22-30(a)) are in good agreement with the adjusted experimental values, whereas figure 22-30(b) shows that the diffusion process for the 723-K specimen is much more rapid than that calculated from the Zn self-diffusion data. If the temperature-time histories for both temperature zones are assumed correct, there seems to be another mass transport mechanism that occurs predominantly in the beginning. This mechanism is not as evident for the longer soak time, because it is obscured by the diffusion process. Because a process other than diffusion obviously occurred, it is not possible to obtain the true diffusion activation energy and the Au diffusion constant from this experiment. Possible transport mechanisms that could lead to the observed results will be considered in the section entitled "Distributions for SF Specimens."

TABLE 22-IV.—T Values for the Four SF Specimens*

Specimen	*Temperature zone, K*	*T*, cm²*
11-A	923	0.39
13-AR	923	.48
21-A	723	.16
17-AR	723	.16

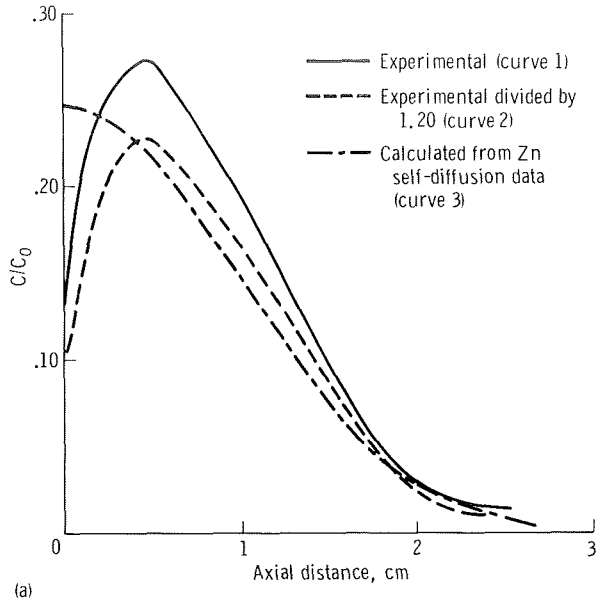

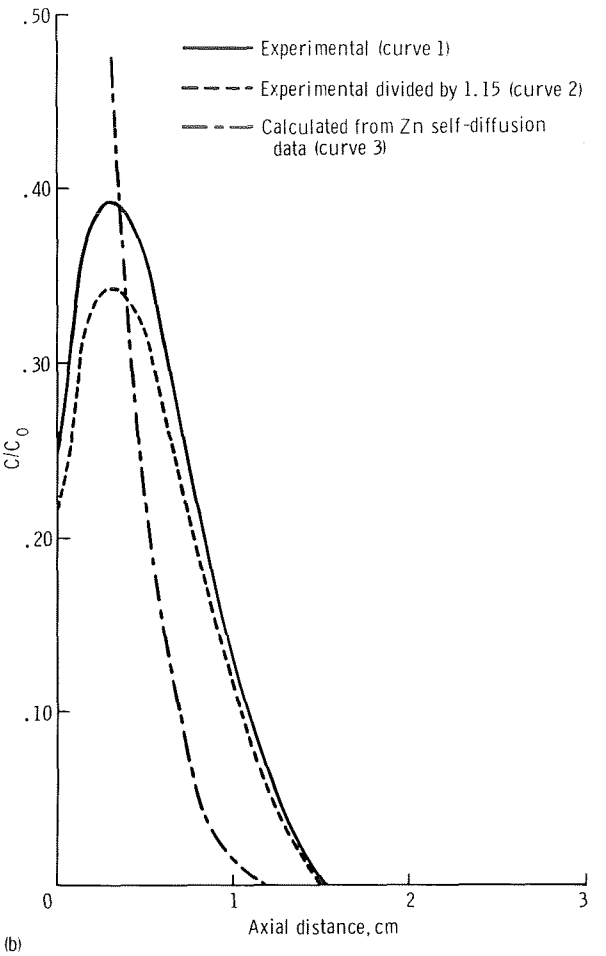

FIGURE 22-30.—Comparison of experimentally determined Au-concentration values with calculated values for SF specimens using Zn self-diffusion data and equation (22-5). (a) Specimen 11-A. (b) Specimen 21-A.

GOLD-CONCENTRATION DETERMINATION FOR GRAPHITE-LINED CONTAINERS

Gold concentration as a function of location was determined by using the Image Data Processing System (IDAPS) at the NASA George C. Marshall Space Flight Center, Huntsville, Alabama, to scan the specimen autoradiographs. Initially, the autoradiograph of the Pb-Au standards, which had been irradiated and autoradiographed with each specimen, was scanned to establish a calibration curve that related transmittance to Au concentration. This scan was done automatically by the computer-based IDAPS. By using the calibration curve, a table that related all gray values for each specimen to Au concentrations was established. This table permitted the output of the densitometer scan of each specimen to be expressed in Au-concentration units rather than gray values. The scanning interval normally used for each specimen was 70 μm, although a scanning interval of 12.5 μm was used for selected magnified regions to examine specimen microstructure. The integration time normally used was 80 microseconds with a signal-to-noise ratio of 34 dB. For the magnifications, an integration time of 1200 microseconds was used with a corresponding signal-to-noise ratio of 46 dB.

The IDAPS provided many possibilities for analyzing the autoradiographs. For this experiment, Au-concentration values for all specimens were obtained and stored on magnetic tape for current and future analyses. For a quick and easier understanding of Au distribution in the specimens, pseudocolors were assigned to particular Au concentration ranges. Using this method, pseudocolor representations showing the Au distribution were obtained. The color scheme used for all specimens is shown in table 22-V.

TABLE 22-V.—Basic Color Scheme Relating Pseudocolors to Au Concentrations

Pseudocolor	*Au concentration, at. p/m*	*Percentage of original Au concentration*
Black	0 to 5	0 to 1.0
Yellow	6 to 10	1.2 to 2.0
Blue-green	11 to 20	2.2 to 4.0
Red	21 to 40	4.2 to 8.0
Green	41 to 80	8.2 to 16.0
Purple	81 to 120	16.2 to 24.0
Dark blue	121 to 160	24.2 to 32.0
Orange	161 to 254	32.2 to 50.8

Distributions for GB Specimens

The pseudocolor representations of the Au distributions in the type AR and A GB specimens are shown in figures 22-31 and 22-32. Figure 22-31(a) shows 923-K specimen 11-AR, in which the original Pb-Au alloy disk was located at the bottom. Each large division shown represents approximately 0.24 cm. As can be seen, a large portion of the Au remained at the bottom. In examining the Au-concentration results, one should be aware that a characteristic of the autoradiographic technique is that an "edge" effect occurs when the radioactive disintegrations are recorded on film. This edge effect is caused by the symmetry of the

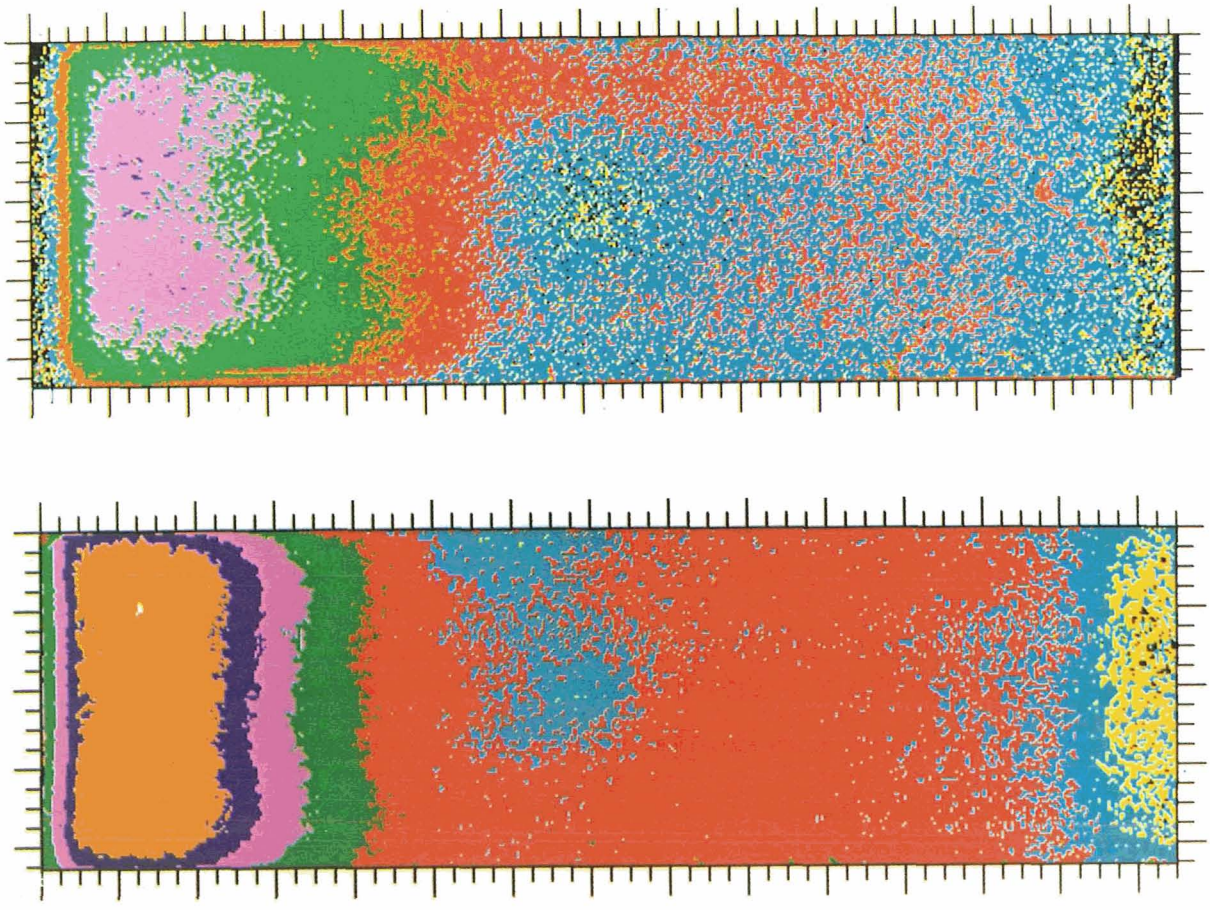

FIGURE 22-31.—Pseudocolor representation of Au concentrations in type AR GB specimens. The pseudocolors are defined in table 22-V. The specimens were mounted vertically in the multipurpose furnace with the original Pb-Au alloy (left side) located at the bottom. The direction of melting was from right to left. (a) Specimen 11-AR; 923-K temperature zone. (b) Specimen 20-AR; 723-K temperature zone.

radioactive disintegrations and is more predominant for β^- particles than for alpha particles because the range of β^- particles in various materials is longer. Thus, at the extreme edge of the samples, the slight decrease in Au concentration recorded is simply a characteristic of the process. The edge effect for all specimens is ≤ 0.4 mm, which is the approximate range of the 960-keV ^{198}Au β^- in Pb.

Thermal soak time for specimen 11-AR (fig. 22-31(a)) was approximately 230 minutes, and it is clearly evident that mixing was incomplete. The flow direction is probably indicated by the red color, and mixing probably occurred in the upper portion of the sample. The pseudocolor representation of the Au distribution for the 723-K GB specimen having the original alloy located at the bottom is shown in figure 22-31(b). Again, it can be seen that most of the Au remained at the bottom of the specimen.

Surprising results were obtained for the GB specimens with the alloy located at the top. Specimens having soak temperatures of 723 and 923 K are shown in figures 22-32(a) and 22-32(b), respectively. Most of the Au "dropped" to the bottom and thus created nearly the same Au distribution for the two temperature zones. Almost identical isograms for the two specimens are shown in figures 22-33(a) and 22-33(b).

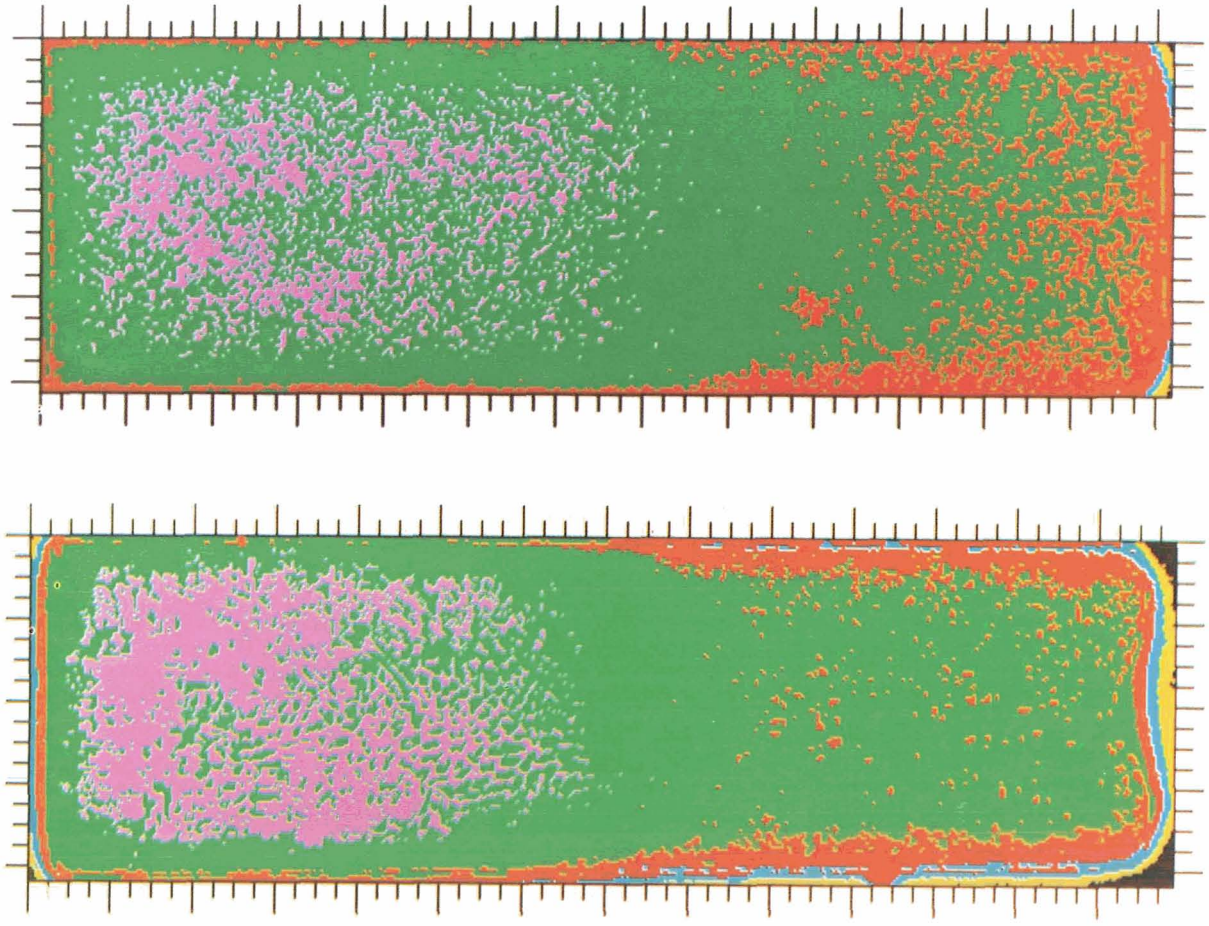

FIGURE 22-32.—Pseudocolor representation of Au concentrations in type A GB specimens. The pseudocolors are defined in table 22-V. The specimens were mounted vertically in the multipurpose furnace with the original Pb-Au alloy (right side) located at the top. The direction of melting was right to left. (a) Specimen 14-A; 723-K temperature zone. (b) Specimen 17-A; 923-K temperature zone.

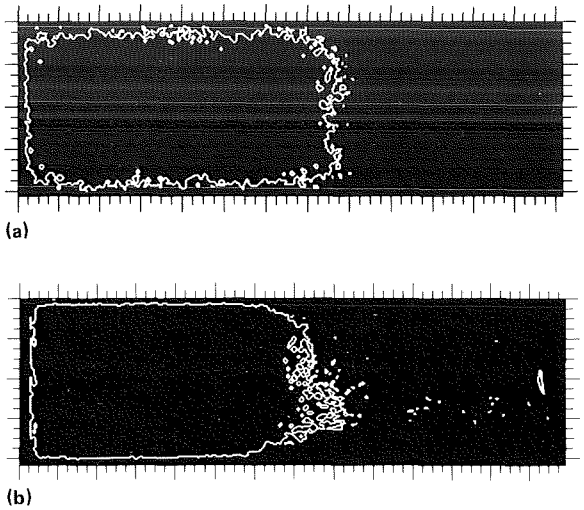

(a)

(b)

FIGURE 22-33.—Isograms showing the 60 at. p/m Au-concentration region for GB specimens. The direction of melting was from right to left. (a) Specimen 14-A; 723-K temperature zone. (b) Specimen 17-A; 923-K temperature zone.

At least two explanations are possible for the Au movement to the bottom in specimens 14-A and 17-A (figs. 22-32(a) and 22-32(b), respectively).

1. Sedimentation effect: This effect is based on the assumption that an equal distribution of Au in the specimen is obtained and that gravity subsequently causes the Au to settle to the bottom. An estimation of this effect shows that the density difference and Au concentrations are below the levels required for the occurrence of sedimentation.

2. System instability: As was shown by Verhoeven (ref. 22-11), fluid systems with heavier materials at the top can sustain only a certain concentration gradient $\Delta C/\Delta Z$ before becoming unstable. The concentration gradient can be obtained from the following equation.

$$\frac{\Delta C}{\Delta Z} = \frac{(R_s)_c \cdot \nu \cdot D}{g \cdot \alpha' \cdot r^4} \qquad (22\text{-}9)$$

where the critical Rayleigh number $(R_S)_C = 68$, the kinematic viscosity $\nu = 1.73 \times 10^{-3}$ cm^2/sec, the diffusion constant $D \approx 4 \times 10^{-5}$ cm^2/sec, the acceleration due to gravity $g = 981$ cm/sec^2, the flow distance $\Delta Z = 2.63 \times 10^3$ cm, r is the radius of the specimen, and $\alpha' = (1/\rho)(d\rho/dC) = 0.4$ where ρ is material density and C is material concentration.

Figure 22-34 is a visual representation of the Pb-Au alloy movement. Because the initial MA-041 concentration gradient was infinite, the Au would be predicted to flow downward to reduce the gradient. Using equation (22-9), one can calculate the Au flow distance required to reach the critical concentration gradient. Calculation of ΔZ yields a predicted distance of 2.6×10^3 cm. Thus, it is highly probable that the movement of the Au was caused by system instability.

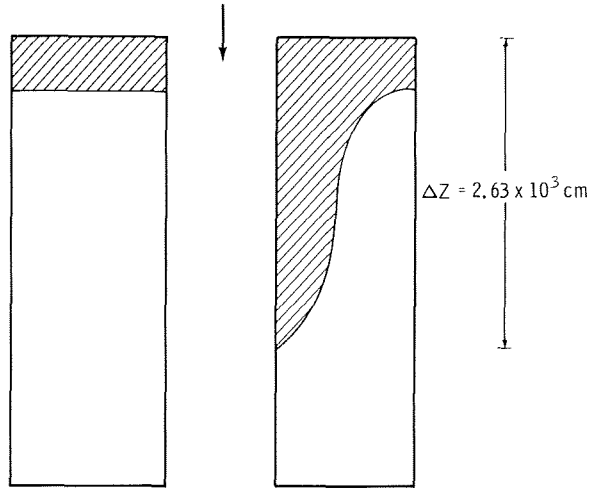

FIGURE 22-34.—Diagram of Pb-Au alloy (shaded) movement to bottom of vertically mounted GB specimens 14-A and 17-A. The diagram is based on the stability analysis of Verhoeven (ref. 22-11) and on equation (22-9).

Distributions for SF Specimens

Gold-concentration pseudocolor representations used for the type A and AR SF specimens from the 923-K temperature zone are shown in figures 22-35(a) and 22-35(b), respectively. For specimen 11-A, the Pb-Au alloy melted first and solidified last; for specimen 13-AR, the alloy melted last and solidified first. Both specimens have curved radial Au concentration profiles with the larger amount of Au at the cylinder axis gradually decreasing toward the wall. Isograms for

specimens 11-A and 13-AR are shown in figures 22-36(a) and 22-36(b), respectively; the isograms show the 5-, 10-, 20-, 40-, and 80-at. p/m Au concentration lines. To the right of the 5-at. p/m concentration line, the concentration decreases to zero; to the left of the 80-at. p/m concentration line, the Au concentration increases to approximately 140 at. p/m for specimen 11-A and to approximately 115 at. p/m for specimen 13-AR. Although about 120 axial Au-concentration profile lines were obtained for each specimen, only the central lines are shown. As can be seen from figures 22-27(a) and 22-27(b), which represent the central axial Au-concentration lines from specimens 11-A and 13-AR, respectively, the Au-diffusion distance for specimen 11-A was slightly greater than that for specimen 13-AR. The ordinates in figures 22-27(a) and 22-27(b) represent the percentage of Au with respect to the initial concentration (500 at. p/m); the amount of Au at any point can be obtained by multiplying the ordinate value by 500. The abscissa values can be converted to distance in millimeters by dividing by 14.5.

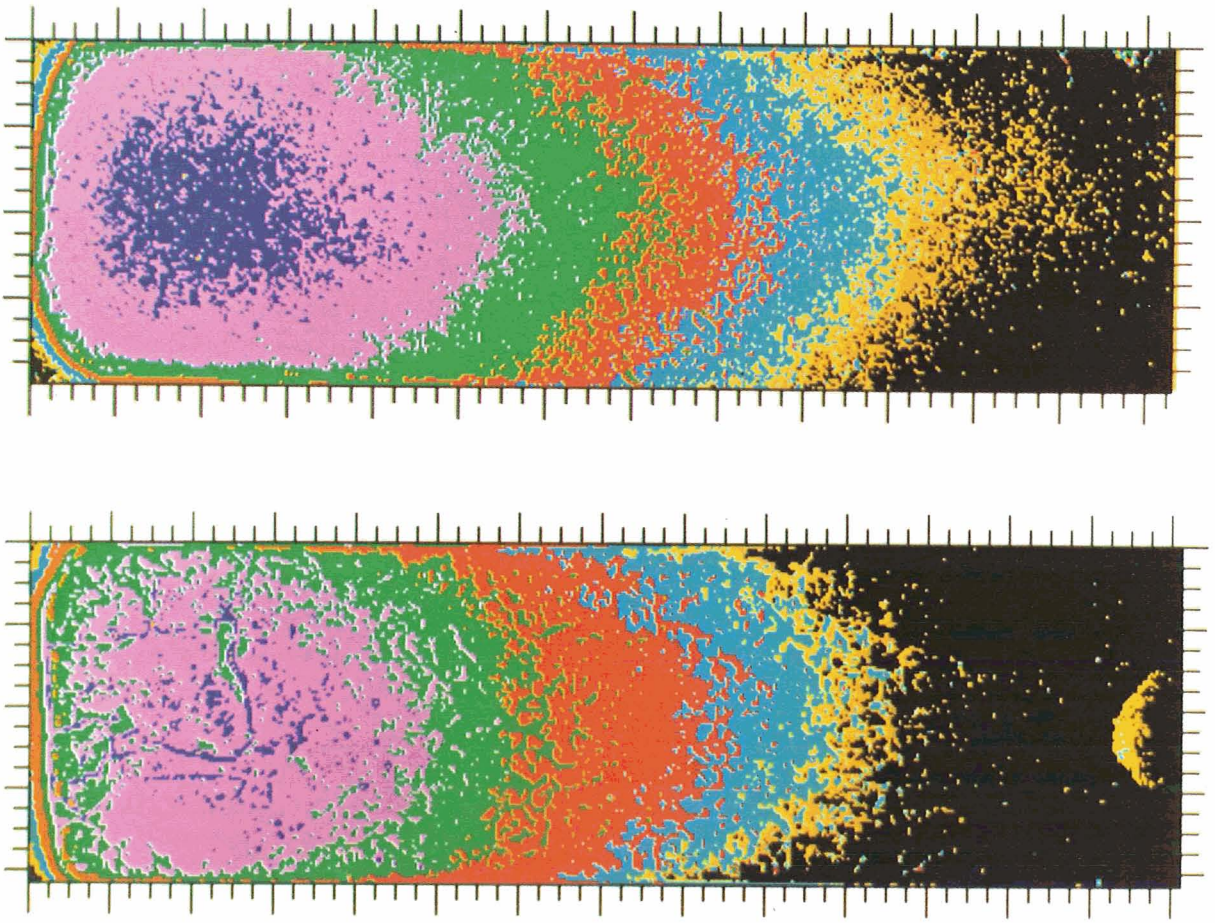

FIGURE 22-35.—Pseudocolor representation of Au concentrations in 923-K SF specimens. The pseudocolors are defined in table 22-V. The original Pb-Au alloy was located on the left-hand side of the specimens. (a) Specimen 11-A; direction of melting was from left to right. (b) Specimen 13-AR; direction of melting was from right to left.

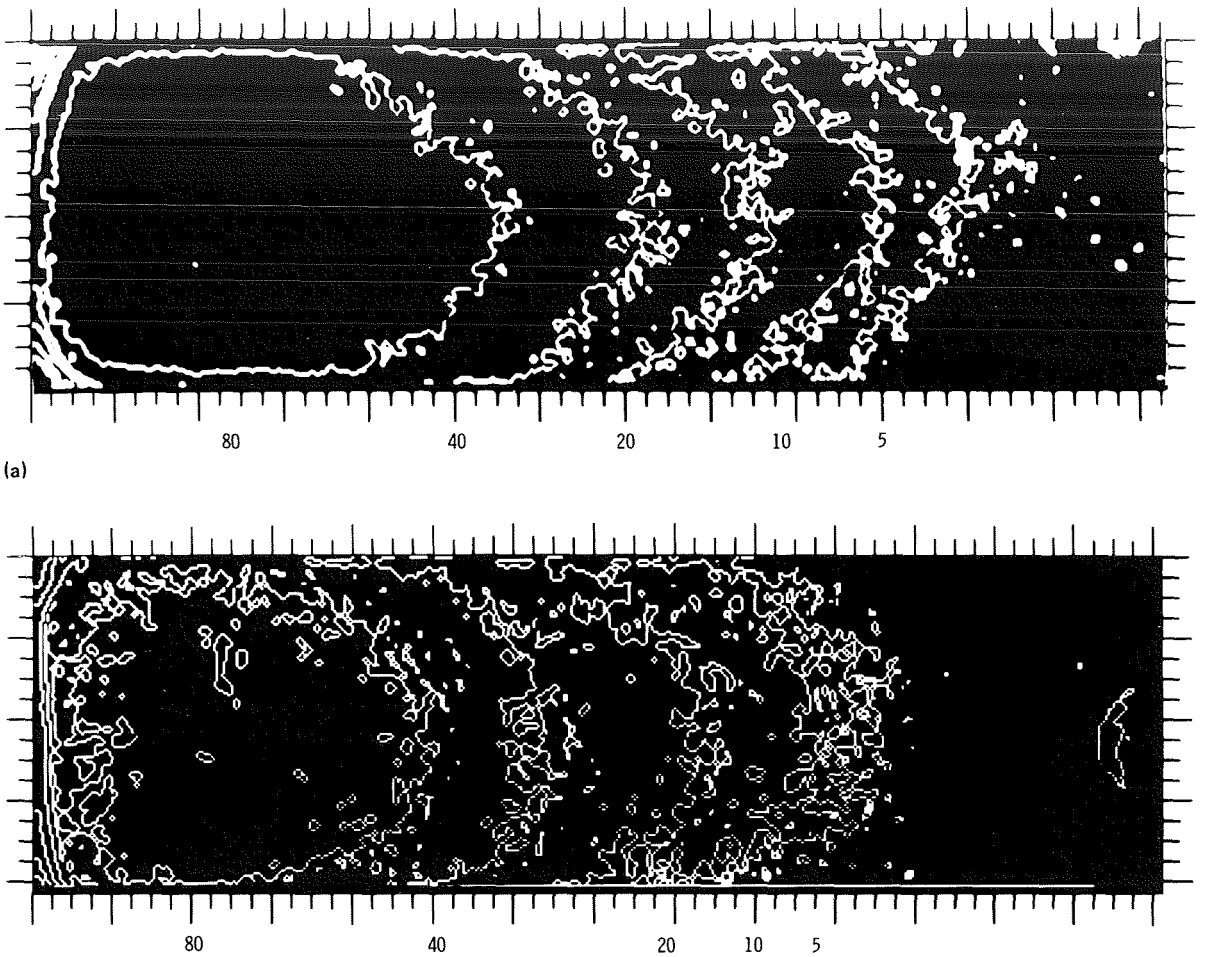

FIGURE 22-36.—Isograms showing the 5-, 10-, 20-, 40-, and 80- at. p/m Au-concentration regions for 923-K SF specimens. (a) Specimen 11-A; direction of melting was from left to right. (b) Specimen 13-AR; direction of melting was from right to left.

Gold-concentration pseudocolor assignments used for SF specimens 21-A and 17-AR, which were located in the 723-K temperature zone of the multipurpose electric furnace, are shown in figures 22-37(a) and 22-37(b), respectively. Gold diffusion into these specimens is approximately equal, as can be seen from the central axial Au-concentration lines shown in figures 22-27(c) and 22-27(d). Curved radial Au-concentration profiles are clearly evident for both specimens, but the curvature appears to be greater for SF specimen 21-A. The only apparent difference between the type A and AR specimens from the 923- and 723-K temperature zones is that the Au-diffusion distance for specimen 13-AR is slightly less than that for specimen 11-A, and the radial concentration curvature is slightly greater for specimen 21-A than for specimen 17-AR. A number of slices were examined for all the SF specimens to determine the location of the maximum Au concentration. The results are shown in table 22-VI. It appears fairly certain that the maximum C/C_0 values

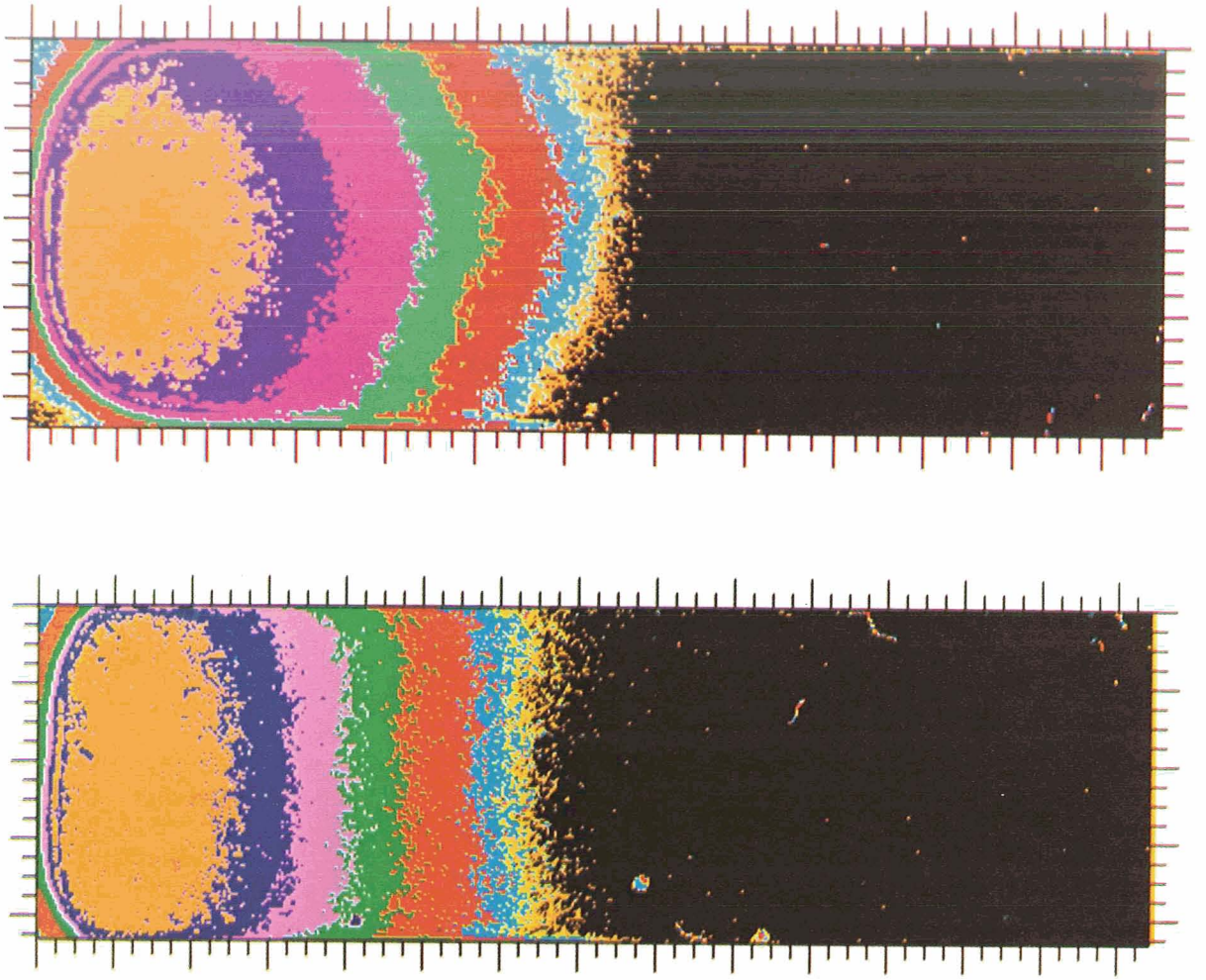

FIGURE 22-37.—Pseudocolor representation of Au concentrations in 723-K SF specimens. The pseudocolors are defined in table 22-V. The original Pb-Au alloy was located on the left-hand side of the specimens. (a) Specimen 21-A; direction of melting was from left to right. (b) Specimen 17-AR; direction of melting was from right to left.

for the 923-K specimens (11-A and 13-AR) were shifted farther into the samples than for the 723-K specimens (21-A and 17-AR).

It appears that the concentration distribution of Au in the SF specimens is not determined simply by diffusion. Independent of the previously discussed diffusion results, there are additional reasons for this conclusion.

1. The occurrence of a maximum Au concentration in the region of the original Pb-Au alloy disk, as shown in table 22-VI

2. The existence of curved Au-concentration profiles in the radial direction for all the SF specimens, as shown in figures 22-35(a), 22-35(b), 22-37(a), and 22-37(b)

3. An increase in the Au concentration in the axial regions

Increase in Au concentration in the axial region was determined by calculating the total Au content in each radial segment and dividing by the initial concentration of the Pb-Au alloy, 500 at. p/m. For example, in figure 22-38(a), the axial Au-concentration increase for SF specimen 11-A is shown. The ordinate represents the total Au content in each segment divided by the initial concentration, and the abscissa shows the location of

TABLE 22-VI.—*Data Used to Locate Maximum Au Concentration*

Segment no.	Longitudinal location, mm	Maximum C/C_0 ratio
Specimen 11-A (923 K)		
6	4.5	0.207
12	4.3	.219
18	4.3	.230
24	4.2	.243
30	4.3	.247
36	4.3	.255
42	4.3	.270
48	4.3	.272
54	4.2	.274
60	4.3	.274
66	4.6	.273
72	4.7	.273
78	4.7	.268
84	4.7	.261
90	4.7	.254
96	4.8	.239
102	4.5	.237
108	4.7	.223
114	4.7	.210
120	4.8	.173
Specimen 21-A (723 K)		
6	3.6	0.270
12	3.4	.304
18	3.4	.324
24	3.4	.342
30	3.3	.352
36	3.2	.360
42	3.2	.388
48	3.1	.388
54	3.1	.389
60	3.1	.395

Segment no.	Longitudinal location, mm	Maximum C/C_0 ratio
Specimen 17-AR (723 K)		
6	3.8	0.329
12	3.9	.349
18	3.4	.363
24	3.4	.365
30	3.3	.370
36	3.3	.370
42	3.3	.374
48	3.2	.379
54	3.1	.379
60	3.1	.378
Specimen 13-AR (923 K)		
6	4.1	0.170
12	4.1	.172
18	5.0	.189
24	4.7	.196
30	4.5	.218
36	4.1	.212
42	5.0	.211
48	5.2	.221
54	5.2	.229
60	5.6	.226
66	5.9	.232
72	6.3	.217
78	6.2	.223
84	4.9	.236
90	5.6	.219
96	5.6	.220
102	4.8	.223
108	4.8	.214
114	4.7	.218
120	4.5	.204

each segment of the specimen with respect to the sample axis, which is set equal to zero. A 20-percent Au-concentration increase in the central region was observed for specimen 11-A (fig. 22-38(a)), with a corresponding concentration decrease in the outer radial portions of the specimen. The axial Au-concentration increases in SF specimens 13-AR, 21-A, and 17-AR are shown in figures 22-38(b), 22-39(a), and 22-39(b), respectively.

The following mechanisms were considered as possible explanations for the Au-concentration distribution in the SF specimens.

1. Melting effects—Radial temperature gradients comparable to longitudinal temperature gradients known to exist might cause variations in Au concentration. Although the magnitudes of the radial temperature gradients are not known, one would expect a difference between the Au-concentration profiles for the type A and AR SF specimens because the melting occurred in opposite directions. However, because the curvature

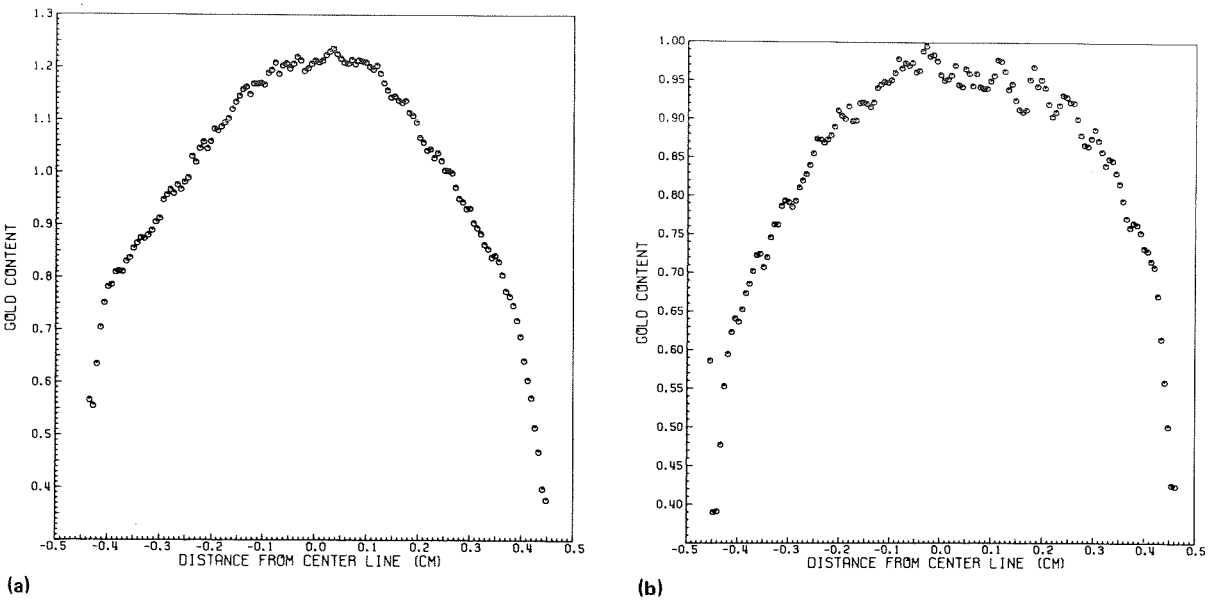

FIGURE 22-38.—Computer printouts showing enhancement of Au in the axial region of 923-K SF specimens. The ordinate represents the percentage of Au for each slice compared to the initial concentration (500 at. p/m). The abscissa represents the radial location of each slice compared to the central slice. (a) Specimen 11-A. (b) Specimen 13-AR.

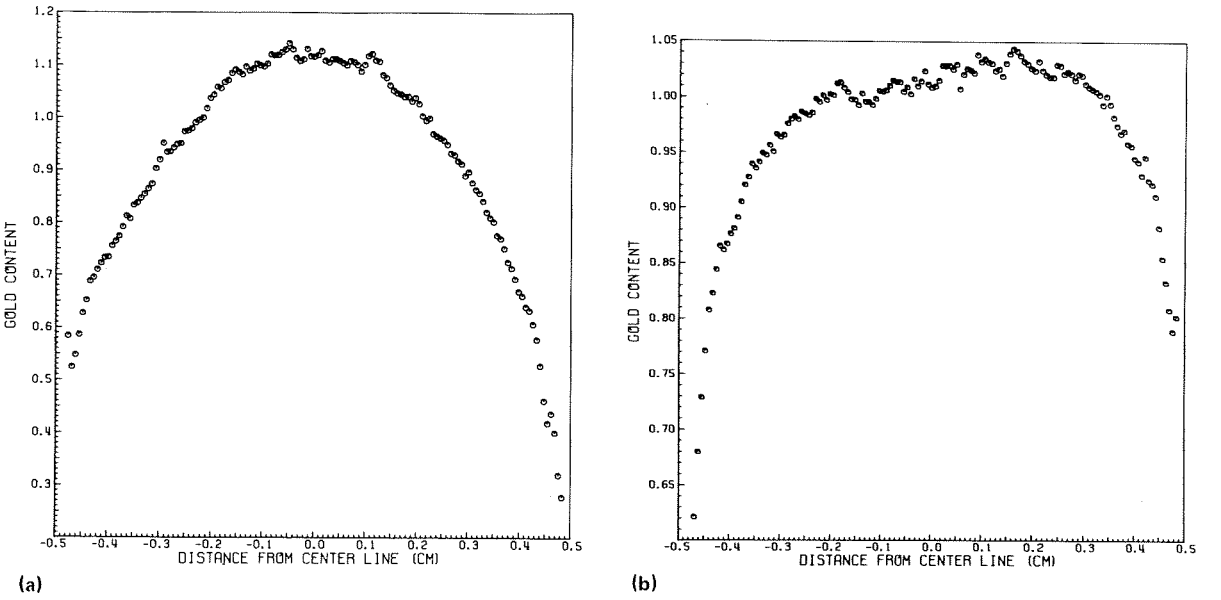

FIGURE 22-39.—Computer printouts showing enhancement of Au in the axial region of 723-K SF specimens. See figure 22-38 for explanation of ordinate and abscissa scales. (a) Specimen 21-A. (b) Specimen 17-AR.

of the Au concentration is the same for both A and AR SF specimens, this explanation is assumed to be invalid.

2. Solidification effects

a. Interdendritic flow—According to Mehrabian et al. (ref. 22-12), the curved concentration profiles could be the result of interdendritic flow. However, an examination of the microstructure revealed no dendritic solidification. Curved Au-concentration profiles were observed even in the low Au-concentration regions (0 to 5 p/m), where dendritic solidification would not be expected. Thus, this explanation seems infeasible.

b. Volume shrinkage—Volume shrinkage during solidification in the presence of curved interfaces generally could cause radial concentration distortion. However, in this case, one would expect opposite radial-concentration-profile curvature for the A and AR specimens. Thus, even though the volume shrinkage for lead is 3.1 percent, it apparently had no effect on the final Au-concentration profiles.

Because the experimental arrangement of the A and AR specimens made it possible to exclude melting or solidification effects as an explanation for the curved Au-concentration profiles, the following mechanisms of flow effects while in the liquid state were considered.

1. Radius-dependent diffusion—Radius-dependent diffusion may occur as the result of a radial temperature gradient. However, if a radial gradient existed because of the furnace design, one would assume a higher temperature at the surface of the specimen. In this case, diffusion would occur more rapidly in the surface region and thus would create a resultant concentration curvature opposite to that observed.

2. Flow caused by gas pressure differences—Pressure difference between the meniscus at the left-hand and right-hand sides of the specimen could cause a flow of all the material in one direction. Therefore, the curved concentration profiles are probably not caused by pressure differential since

a. All material would necessarily flow in the same direction.

b. The specimens were sealed in the ampoules at a very low pressure (0.133 mN/m^2 (1×10^{-6} torr)).

3. Meniscus-forming induced flow—Meniscus-induced flow could have contributed to forming the curved Au-concentration profiles. The equilibrium form of the meniscus in a nonwetting container under zero-g conditions is a half sphere. Under this assumption, during the melting process, some material from the outer region would flow to the central region to form the equilibrium shape. Material flow would occur toward the center of the specimen, and part of the material would flow back and form the flow patterns shown in figure 22-40. In Experiment MA-041, such an effect was probably less significant than other effects because the development of the meniscus was impeded by the confining walls of the capsule.

4. Marangoni-effect induced flow—Experimental results can be explained by assuming that induced material flow was caused by either a difference in the interfacial energies between the alloy-graphite or lead-graphite, or a difference in the surface tensions of the alloy and pure Pb according to the contact conditions discussed later. Assuming the interfacial tension of alloy-graphite to be greater than that of Pb-graphite, convection could occur after melting in the region and in the direction shown in figure 22-41 to decrease the difference in the interfacial tensions or the surface tensions. Lead would be transported in the region near the walls to the alloy region and thus would dilute the latter region. A corresponding flow would occur in the specimen center in the opposite direction and would cause the alloy to flow into the pure-Pb region.

An estimate of the Marangoni number M_a was obtained from the equation

$$M_a = -\Delta\gamma \frac{L}{\eta\psi} \qquad (22\text{-}10)$$

where $\Delta\gamma$ is the surface tension difference, L is the specimen diameter, η is viscosity, and ψ is

heat diffusivity defined as

$$\psi = \frac{\lambda}{\rho c_v} \qquad (22\text{-}11)$$

where λ is heat conductivity, ρ is density, and c_v is specific heat at constant volume.

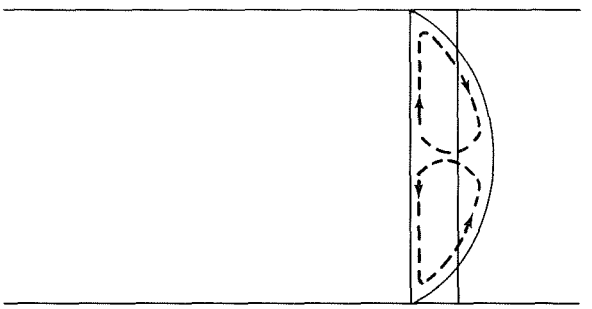

FIGURE 22-40.—Schematic representation of the flow pattern for meniscus-forming induced flow.

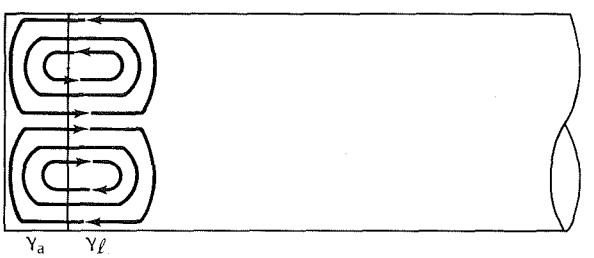

FIGURE 22-41.—Schematic representation of the flow patterns arising from the Marangoni effect, where γ_a and γ_l represent the surface tension of the Pb-Au alloy and of pure Pb, respectively.

Estimation of the Marangoni number was made using available surface tension values of the similar copper-tin system and assuming a surface tension difference of 0.37×10^{-5} N/cm (0.37 dyn/cm) and a specimen diameter of 1 cm. The estimated value of 97 for the 723-K specimens supports the preceding argument because the critical Marangoni number for zero gravity is zero.

The Marangoni effect can, in fact, be responsible for all the experimental observations, such as the Au-concentration minimums, the occurrence of an Au-concentration maximum not at the beginning of the alloy as in a normal diffusion experiment but at some distance from the end of the specimen, and the low Au concentrations in the outer radial regions of the specimens. In addition, smaller curvatures for the lower temperature specimens can be explained by the same mechanism, because the greater viscosity at the lower temperature would result in a lower flow velocity.

Additional support for induced flow resulting from the Marangoni effect can be found in at least three other experiments.

1. Indium self-diffusion under normal gravity conditions (ref. 23-13)—The capillary method was used to study indium self-diffusion over a wide temperature range. Curved concentration profiles were observed. Nachtrieb (ref. 22-10, p. 314) attributed these results to radial segregation of the indium tracer isotope. On the basis of isotope separation theory, the investigators believe that this explanation is very unlikely.

2. Liquid Zn self-diffusion under near-zero-g conditions (ref. 22-5)—Zinc-65 was pressure bonded to Zn and placed inside a carbon-lined tantalum ampoule. Samples remained in the liquid state for 1 hour. Zinc-65 concentration profiles were determined by sectioning the specimens and gamma-counting each segment to determine the ^{65}Zn concentration. Results indicated curved concentration profiles in the radial direction attributed by Ukanwa to surface diffusion, capillary attraction, or some sort of surface phenomena.

3. Tea diffusion experiment under near-zero-g conditions (ref. 22-14)—A tea solution was placed in an ampoule containing water, and the diffusion process was monitored. Curved concentration profiles were visually observed by the Skylab astronauts, but no quantitative data were obtained.

The investigators believe that the results of the first two experiments can better be explained by

Marangoni-effect induced flow resulting from surface tension gradients induced by temperature gradients, and that the interfacial or surface tension gradient in the third experiment was caused by concentration differences. The greatest flaw in the preceding explanation is that, according to hydrodynamic theories, Marangoni-effect induced flow should only occur on "free" surfaces. In Experiment MA-041 and the three experiments described previously, it must be assumed that the liquid touched the container walls. Thus, flow caused by interfacial tension gradients can only occur if one assumes a nonzero flow velocity at the walls. According to Scriven[2] and Richardson (ref. 22-4), such an assumption is a violation of the zero-slip boundary condition. On the other hand, the investigators believe that some reasons exist for doubting the applicability of zero-slip boundary conditions in space. The degree of contact of the nonwetting fluid may be different for null gravity than for normal gravity. The fluid may have only partly contacted the ampoule wall; thus, free surfaces could have existed over small regions. The degree of contact is influenced by the different pressures in the fluid. If, in fact, the Marangoni-effect induced flow in Experiment MA-041 was not hindered by total contact, one can assume, in this case, that flow was caused by the difference in the surface tensions rather than in the interfacial tensions.

The best explanation at this time for the experimental results is that a flow induced by the Marangoni effect did occur. The investigators suggest that studies should be made concerning the validity of the nonzero boundary condition in zero gravity with nonwetting materials and different surface structures for the container walls.

GOLD-CONCENTRATION DETERMINATION FOR MILD STEEL CONTAINERS

The Au-concentration distribution for the specimens in mild steel containers was similar to that determined for the specimens in graphite-lined containers. Macrographs of the longitudinally sectioned surfaces of mild-steel-contained GB and SF specimens are shown in figures 22-42 to 22-44. As shown by the meniscus shapes, the contact angle in all cases is $>90°$. Rough measurements of contact angles indicate a tendency for nonwetting for the GB specimens and nearly total nonwetting for the SF specimens.

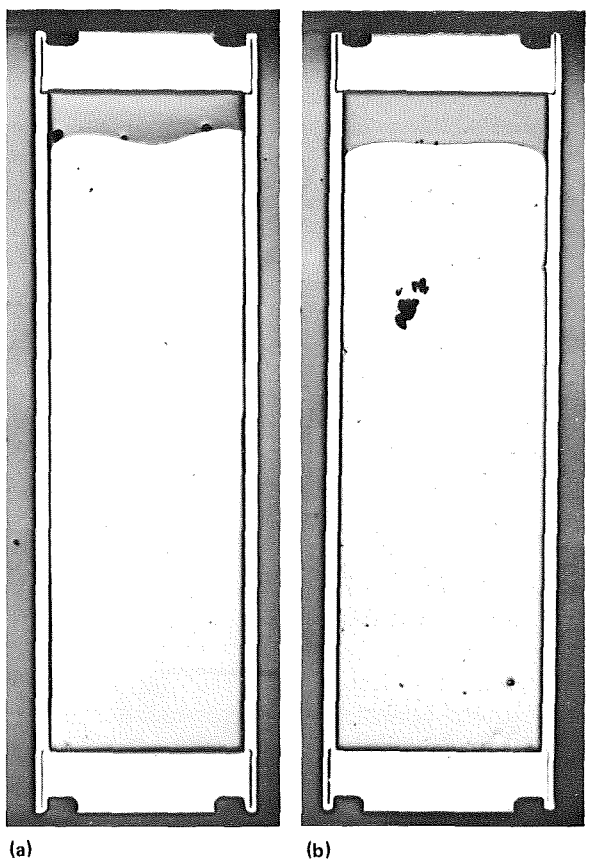

FIGURE 22-42.—Macrographs of metallographically polished, longitudinally sectioned surfaces of GB specimens contained in mild steel ampoules. The specimens were mounted vertically. The original Pb-Au alloy was located at the top. The direction of melting was from top to bottom. (a) Specimen 13-B; 923-K temperature zone. (b) Specimen 15-B; 723-K temperature zone.

[2]L. E. Scriven, personal communication, July 1976.

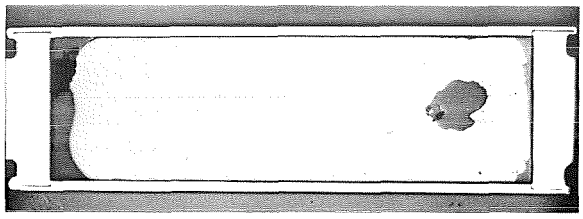

FIGURE 22-43.—Macrograph of metallographically polished, longitudinally sectioned surface of SF specimen 12-B contained in a mild steel ampoule. The specimen was located in the 923-K temperature zone and melted from left to right. The original Pb-Au alloy was located in the vicinity of the large void.

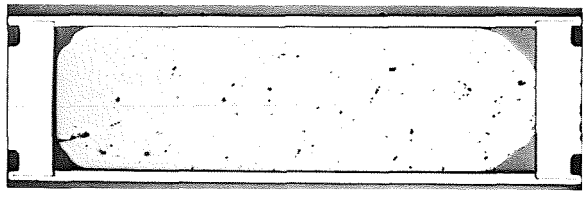

FIGURE 22-44.—Macrograph of metallographically polished, longitudinally sectioned surface of SF specimen 21-B contained in a mild steel ampoule. The specimen was located in the 723-K temperature zone and melted from left to right. The original Pb-Au alloy was located on the left-hand side of the specimen. Dark spots are oxide deposits on the surface.

EXAMINATION OF SPECIMEN MICROSTRUCTURES

Initial investigations revealed no systematic differences between the microstructures of the GB and SF specimens. Selected areas in the autoradiographs of two SF specimens and one GB specimen were magnified for an examination of the microstructure. The observed microstructures can be classified as follows.

1. Grain and subgrain boundaries
2. Well-developed cell structure
3. Diffuse (little structure)

Examples of these classifications are shown in figures 22-45, 22-46, and 22-47, respectively. Each large division in the figures represents approximately 0.7 mm.

Figure 22-45 is an enlargement of a selected area in the Au-rich region of figure 22-35(b) (SF specimen 13-AR) that contains grain and subgrain boundaries. The pseudocolor assignment is as shown in table 22-V. Segregation of Au at the grain boundaries is shown by the orange and represents at least a 60-percent increase over the amount of Au in the adjacent grain region. One also can observe that segregation in the grain boundaries is not homogeneous.

Well-developed cell structure is shown in figure 22-46, which is an enlargement of a selected area in the center of figure 22-32(b) (GB specimen 17-A). The pseudocolor assignment for the Au concentrations in figure 22-46 is shown in table 22-VII. Quantitative Au-concentration data for the magnified region of GB specimen 17-A are shown in figure 22-48 for a slice taken parallel to the melting direction. The slice analyzed in figure 22-48 was located approximately 9.5 large divisions from the top of figure 22-32(b). The average cell size calculated from the slice is approximately 0.3 mm. In addition, further examination of the slice reveals a segregation increase of Au at the cell walls of approximately 50 percent compared to the cell interior. Both figures 22-46 and 22-48 reveal that the cell walls are not very sharp; the walls are broadened either during formation or by diffusion in the solid.

An enlargement of a selected area in the Au-rich region of SF specimen 11-A (fig. 22-35(a)) is shown in figure 22-47 to illustrate diffuse microstructure. The pseudocolor representation of the Au concentrations for this magnification is shown in table 22-VII. As one can see, very little structure is present.

Results obtained for the three magnifications represent only a beginning in the examination of the microstructure of both GB and SF specimens.

SUMMARY

The purpose of the Surface-Tension-Induced Convection Experiment was to observe compositional-induced convection effects. Convection effects were observed but were not sufficiently large to bring about total mixing in the SF specimens. However, they were large enough to prohibit analysis of the pure diffusion process. The most plausible explanation for the flow phenomena observed is convection induced by

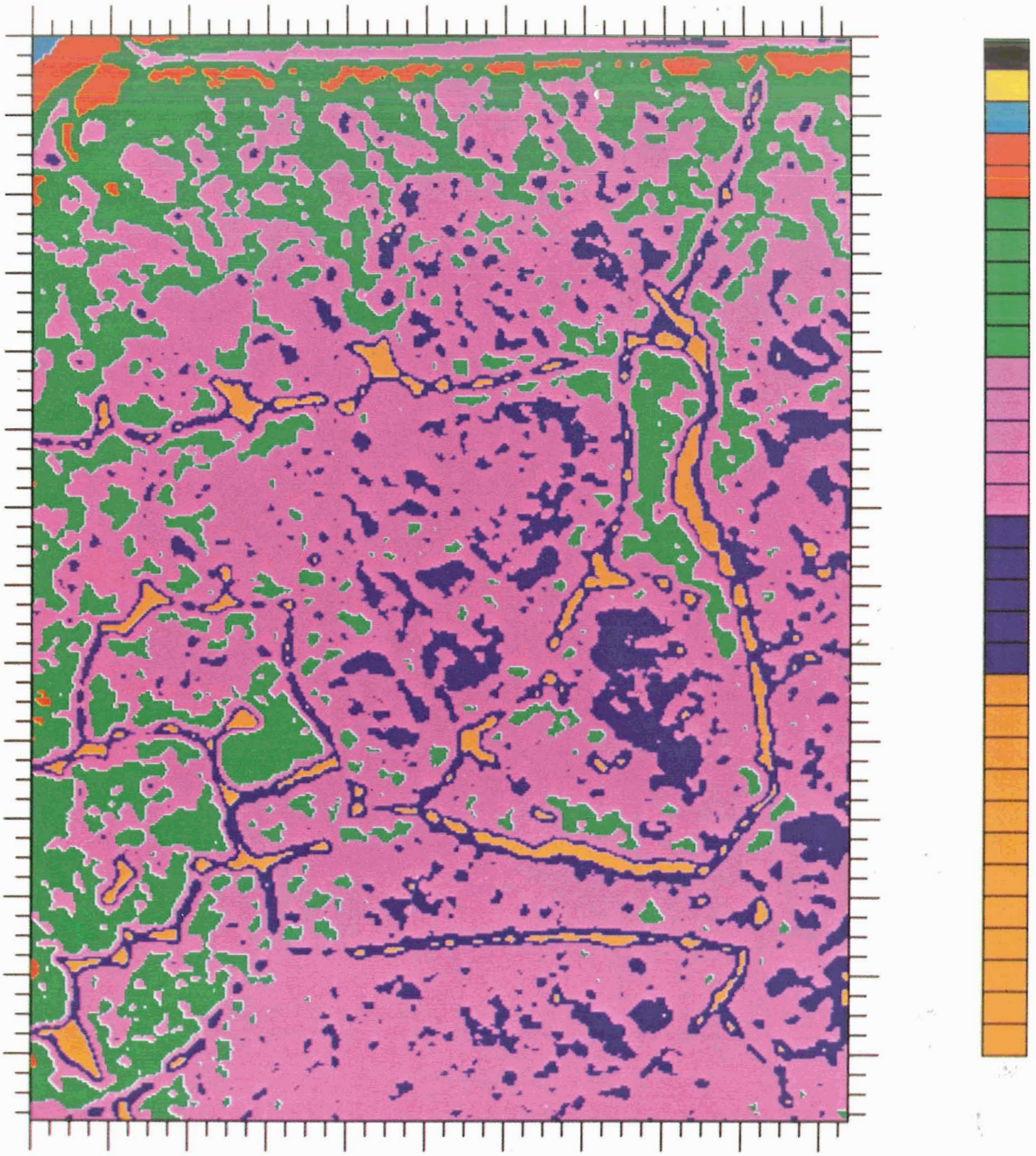

FIGURE 22-45.—Enlarged pseudocolor representation of Au-rich region of 923-K SF specimen 13-AR showing grain and subgrain boundaries. The pseudocolors are defined in table 22-V. The direction of melting was from right to left.

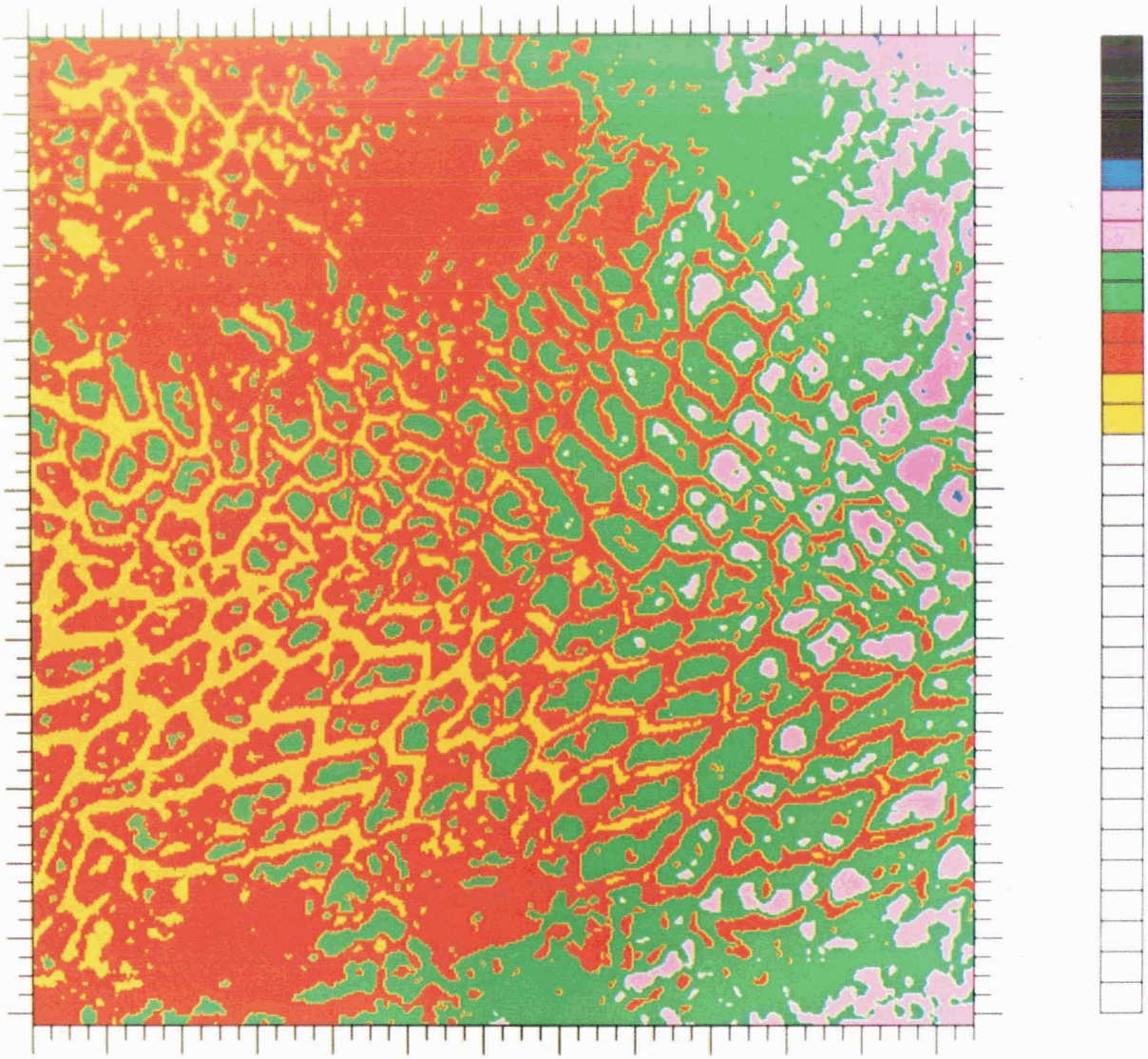

FIGURE 22-46.—Enlarged pseudocolor representation of an area of 923-K GB specimen 17-A showing well-developed cell structure. The pseudocolor Au-concentration assignments are shown in table 22-VII. The direction of melting was from right to left.

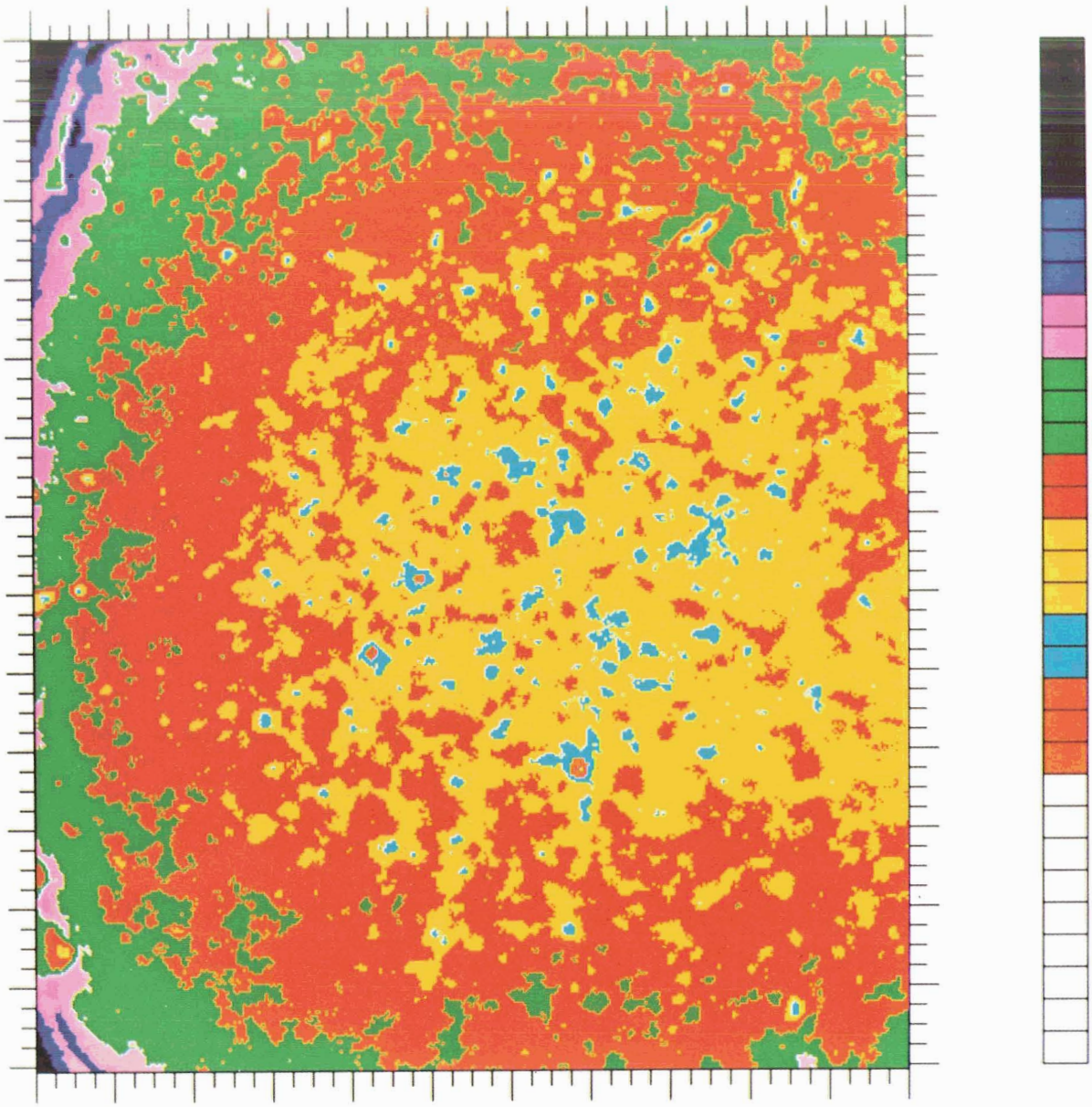

FIGURE 22-47.—Enlarged pseudocolor representation of an area of 923-K SF specimen 11-A showing the lack of cell structure characteristic of diffusion. The pseudocolor Au-concentration assignments are shown in table 22-VII. The direction of melting was from left to right.

TABLE 22-VII.—Pseudocolor Au-Concentration Assignments for Magnifications

Pseudocolor	*Au concentration, at. p/m*	*Percentage of original Au concentration*
	GB specimen 17-A	
Black	0 to 24	0 to 4.0
Blue	25 to 40	5.0 to 8.0
Pink	41 to 55	8.2 to 11.0
Green	56 to 70	11.2 to 14.0
Red	71 to 85	14.2 to 17.0
Yellow	86 to 100	17.2 to 20.0
	SF specimen 11-A	
Black	0 to 40	0 to 8.0
Dark blue	41 to 60	8.2 to 12.0
Purple	61 to 80	12.2 to 16.0
Green	81 to 100	16.2 to 20.0
Red	101 to 120	20.2 to 24.0
Yellow	121 to 140	24.2 to 28.0
Light blue	141 to 160	28.2 to 32.0
Red-brown	161 to 180	32.2 to 36.0

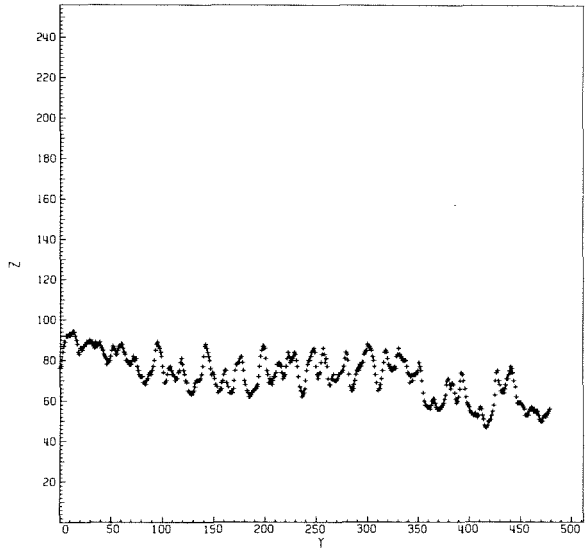

FIGURE 22-48.—Computer printout showing Au-concentration data for a slice parallel to the melting direction of GB specimen 17-A (fig. 22-46). The ordinate represents the Au concentration in atomic parts per million; the abscissa represents the column number, where the corresponding linear distance between two columns on the sample slice is 0.0175 mm.

the Marangoni effect; if this explanation is in fact correct, a violation of the no-slip boundary condition must be assumed. Results for the GB specimens were totally different from those obtained in space; convection was a dominant factor in the GB specimen mixing.

Expected wetting of the mild steel capsules did not occur in space, and only a partial wetting occurred for the GB specimens.

Initial investigation of the microstructures revealed no systematic differences between GB and SF specimens. Segregation resulted in an increase in Au concentration of approximately 50 to 60 percent in the cell walls and grain boundaries.

REFERENCES

22-1. Grodzka, P. G.; and Bannister, T. C.: Natural Convection in Low-g Environments. AIAA Paper 74-156, 1974.

22-2. Larson, D. J.: Skylab M553 Sphere Forming Experiment. Proceedings of the 3rd Space Processing Symposium on Skylab Results, Vol. 1. NASA TM X-70252, 1974, pp. 101-113.

22-3. McKannan, E. C.; and Poorman, R. M.: Skylab M551 Metals Melting Experiment. Proceedings of the 3rd Space Processing Symposium on Skylab Results, Vol. 1. NASA TM X-70252, 1974, pp. 85-100.

22-4. Richardson, S.: On the No-Slip Boundary Condition. J. Fluid Mech., vol. 59, pt. 4, Aug. 7, 1973, pp. 707-719.

22-5. Ukanwa, A. O.: M558 Radioactive Tracer Diffusion. Proceedings of the 3rd Space Processing Symposium on Skylab Results, Vol. 1. NASA TM X-70252, 1974, pp. 425-456.

22-6. Semenchenko, V. K. (N. G. Anderson, transl.; R. Kennedy, ed.): Surface Phenomena in Metals and Alloys. Pergamon Press Ltd. (London), 1962.

22-7. Hansen, Max: Constitution of Binary Alloys. McGraw-Hill Book Company (New York), 1958.

22-8. Reed, R. E.: Redistribution of Tantalum and Tungsten Impurities in Niobium by Electron Beam Float Zone Refining. J. Crystal Growth, vol. 19, no. 1, 1973, pp. 61-64.

22-9. Crank, J.: The Mathematics of Diffusion. Oxford University Press (London), 1956.

22-10. Nachtrieb, N. H.: Self-Diffusion in Liquid Metals. The Properties of Liquid Metals. Proceedings of the International Conference Held at Brookhaven National Laboratory, Upton, New York, Sept. 1966. Taylor & Francis, Ltd. (London), 1967, pp. 309-323.

22-11. Verhoeven, J. D.: Convection Effects in the Capillary Reservoir Technique for Measuring Liquid Metal Diffusion Coefficients. Trans. Met. Soc. AIME, vol. 242, no. 9, Sept. 1968, pp. 1937-1942.

22-12. Mehrabian, R.; Keane, M.; and Flemings, M. C.: Interdendritic Fluid Flow and Macrosegregation; Influence of Gravity. Met. Trans., vol. 1, no. 5, May 1970, pp. 1209-1220.

22-13. Careri, G.; Paoletti, A.; and Vincentini, M.: Further Experiments on Liquid Indium and Tin Self-Diffusion. Nuovo Cimento, vol. 10, 1958, pp. 1088-1099.

22-14. Bannister, Tommy C.: Science Demonstrations on Skylab in the Material Processing Area. Proceedings of the 3rd Space Processing Symposium on Skylab Results, Vol. 1. NASA TM X-70252, 1974, pp. 491-595.

IN MEMORIAM

Dr. Richard E. Reed, Principal Investigator for the MA-041 Experiment, exhibited unusual dedication by his continuous participation in this investigation until his untimely death. His colleagues and associates remember him for his unrelenting adherence to the highest stardards of scientific research.